

Central Lancashire Online Knowledge (CLoK)

Title	Witnessing the fragmentation of a filament into prestellar cores in Orion B/NGC 2024?
Type	Article
URL	https://clock.uclan.ac.uk/45464/
DOI	https://doi.org/10.1051/0004-6361/202140857
Date	2023
Citation	Shimajiri, Y., Andre, Ph., Peretto, N., Arzoumanian, D., Ntormousi, E. and Konyves, Vera (2023) Witnessing the fragmentation of a filament into prestellar cores in Orion B/NGC 2024? <i>Astronomy & Astrophysics (A&A)</i> , 672. ISSN 0571-7256
Creators	Shimajiri, Y., Andre, Ph., Peretto, N., Arzoumanian, D., Ntormousi, E. and Konyves, Vera

It is advisable to refer to the publisher's version if you intend to cite from the work.
<https://doi.org/10.1051/0004-6361/202140857>

For information about Research at UCLan please go to <http://www.uclan.ac.uk/research/>

All outputs in CLoK are protected by Intellectual Property Rights law, including Copyright law. Copyright, IPR and Moral Rights for the works on this site are retained by the individual authors and/or other copyright owners. Terms and conditions for use of this material are defined in the <http://clock.uclan.ac.uk/policies/>

Witnessing the fragmentation of a filament into prestellar cores in Orion B/NGC 2024^{★,★★}

Y. Shimajiri^{1,2,3}, Ph. André³, N. Peretto⁴, D. Arzoumanian^{2,5,6}, E. Ntormousi^{7,8}, and V. Könyves⁹

¹ Kyushu Kyoritsu University, Jiyugaoka 1–8, Yahatanishi-ku, Kitakyushu, Fukuoka 807-8585, Japan
e-mail: y-shimajiri@fains.jp

² National Astronomical Observatory of Japan, Osawa 2-21-1, Mitaka, Tokyo 181-8588, Japan

³ Laboratoire d'Astrophysique (AIM), Université Paris-Saclay, Université Paris Cité, CEA, CNRS, AIM, 91191 Gif-sur-Yvette, France

⁴ Cardiff University, School of Physics & Astronomy, Queen's buildings, The parade, Cardiff CF24 3AA, UK

⁵ Instituto de Astrofísica e Ciências do Espaço, Universidade do Porto, CAUP, Rua das Estrelas, 4150-762 Porto, Portugal

⁶ Aix Marseille Univ., CNRS, CNES, LAM, Marseille, France

⁷ Scuola Normale Superiore, Piazza dei Cavalieri 7, 56126 Pisa, Italy

⁸ Foundation for Research and Technology (FORTH), Nikolaou Plastira 100, Vassilika Vouton, 711 10 Heraklion, Greece

⁹ Jeremiah Horrocks Institute, University of Central Lancashire, Preston PR1 2HE, UK

Received 22 March 2021 / Accepted 23 January 2023

ABSTRACT

Context. Recent *Herschel* observations of nearby molecular clouds have shown that filamentary structures are ubiquitous and that most prestellar cores form in dense filaments. Probing the detailed density and velocity structure of molecular filaments is therefore crucial for improving our observational understanding of the star formation process.

Aims. We aim to characterize both the density and the velocity field of a typical molecular filament in the process of fragmenting into cores.

Methods. We mapped a portion of the NGC 2024 region in the Orion B molecular cloud with the Nobeyama 45m telescope, in the ¹²CO ($J=1-0$), ¹³CO ($J=1-0$), C¹⁸O ($J=1-0$), and H¹³CO⁺ ($J=1-0$) lines, and the southwestern part of NGC 2024, corresponding to the NGC 2024S filament, with the NOthern Extended Millimeter Array (NOEMA) interferometer in H¹³CO⁺ ($J=1-0$).

Results. The maps of ¹³CO, C¹⁸O, and H¹³CO⁺ emission trace at least part of the filamentary structure seen in the 8'' resolution ArTéMiS+*Herschel* data. The median radial column density profile of the NGC 2024S filament as derived from ArTéMiS+*Herschel* dust emission data is well fitted by a Plummer profile with a half-power diameter $D_{\text{HP}}^{\text{Plummer}} = 0.081 \pm 0.014$ pc, which is similar to the findings of previous studies of nearby molecular filaments with *Herschel*. On the other hand, the half-power diameters of NGC 2024S as measured from the Nobeyama ¹³CO and C¹⁸O data are broader than, and the half-power diameter derived from the H¹³CO⁺ data narrower than the filament diameter measured with *Herschel*. These results suggest that the ¹³CO and C¹⁸O data trace only the (low-density) outer part of the *Herschel* filament and the H¹³CO⁺ data only the (dense) inner part. We identify four cores in the portion of the *Herschel* map covered by NOEMA and find that each *Herschel* core corresponds to a single core detected in the combined NOEMA+45m H¹³CO⁺ data cube. The Nobeyama H¹³CO⁺ centroid velocity map reveals velocity gradients along both the major and the minor axis of the NGC 2024S filament, as well as velocity oscillations with a period $\lambda \sim 0.2$ pc along the major axis. Comparison between the centroid velocity and the column density distribution shows a tentative $\lambda/4$ phase shift in H¹³CO⁺ or C¹⁸O. This $\lambda/4$ shift is not simultaneously observed for all cores in any single tracer but is tentatively seen for each core in either H¹³CO⁺ or C¹⁸O. The difference between the H¹³CO⁺ and C¹⁸O velocity patterns may arise from differences in the range of densities probed by H¹³CO⁺ and C¹⁸O. We produced a toy model that takes into account the three velocity-field components: a transverse velocity gradient, a longitudinal velocity gradient, and a longitudinal oscillation mode caused by fragmentation. Examination of synthetic data shows that the longitudinal oscillation component produces an oscillation pattern in the velocity structure function of the model. Since the velocity structure function of the Nobeyama H¹³CO⁺ centroid velocity data does show an oscillation pattern, we suggest that our observations are partly tracing core-forming motions and the fragmentation of the NGC 2024S filament into cores. We also find that the mean core mass in NGC 2024S corresponds to the effective Bonnor-Ebert mass in the filament. This is consistent with a scenario in which higher-mass cores form in higher-line-mass filaments.

Key words. stars: formation – molecular data – ISM: clouds

1. Introduction

Molecular clouds have long been known to exhibit long filamentary structures (e.g., Schneider & Elmegreen 1979). *Herschel* observations have confirmed that such filaments are truly ubiquitous in the cold interstellar medium of the Milky Way (e.g., Molinari et al. 2010; Arzoumanian et al. 2011, 2019; Palmeirim et al. 2013; Cox et al. 2016; Schisano et al. 2020). Filaments are observed in both actively star-forming and

* Reduced datacubes and images are also available at the CDS via anonymous ftp to cdsarc.cds.unistra.fr (130.79.128.5) or via <https://cdsarc.cds.unistra.fr/viz-bin/cat/J/A+A/672/A133>

** Partly based on observations carried out with the IRAM NOEMA Interferometer under project number W16AC. IRAM is supported by INSU/CNRS (France), MPG (Germany) and IGN (Spain).

quiescent, non-star-forming molecular clouds (see André et al. 2010; Miville-Deschênes et al. 2010). The *Herschel* observations also show that the typical width of nearby filaments (< 500 pc) measured in H_2 column density maps is ~ 0.1 pc with a factor of ~ 2 dispersion around this value (Arzoumanian et al. 2011, 2019). There has been some debate about the reliability of this finding (Panopoulou et al. 2017, 2022; Hacar et al. 2022), but tests performed on synthetic data suggest that *Herschel* width measurements are free from significant biases, at least in the case of nearby, high-contrast filamentary structures (Roy et al. 2019; Arzoumanian et al. 2019; André et al. 2022). While identifying a robust theoretical model for the origin of this typical filament width has been difficult (e.g. Hennebelle & André 2013; Ntormousi et al. 2016), a promising albeit incomplete idea suggests a connection with the magneto-sonic scale of interstellar turbulence in diffuse molecular gas (Federrath 2016). Given the debate, it is very valuable to keep exploring filament widths further with new observational analyses.

The formation mechanism of molecular filamentary structures is not fully understood (cf. Pineda et al. 2022, for a review), but there is some evidence that molecular filaments may form and grow within sheet-like structures resulting from the compression of interstellar matter by large-scale shock waves (Palmeirim et al. 2013; Arzoumanian et al. 2018; Shimajiri et al. 2019b; Chen et al. 2020; Bonne et al. 2020). Observations with *Herschel* have also shown that most prestellar cores are embedded within dense molecular filaments (e.g. André et al. 2010; Könyves et al. 2015, 2020; Marsh et al. 2016), suggesting that molecular filaments are the main sites of at least low-to intermediate-mass star formation. In a particular case in Taurus, direct kinematic evidence of core-forming motions along a filament has even been reported, thanks to observations with the Institut de radioastronomie millimétrique (IRAM) 30m telescope, in the form of coherent velocity and density oscillations with a $\lambda/4$ phase shift between the density and the velocity field (Hacar & Tafalla 2011). Mostly based on *Herschel* results, André et al. (2014) proposed a scenario for star formation in filaments whereby large-scale compression of interstellar material in supersonic flows generates a complex web of ~ 0.1 -parsec-wide filaments in the cold interstellar medium, and these filaments then fragment into prestellar cores due to gravitational instability. This scenario has the merit that it may possibly account for the “base” of the prestellar core mass function and by extension the stellar initial mass function for $0.1 M_\odot \lesssim M_\star \lesssim 1 M_\odot$. In particular, there is evidence that molecular filaments may fragment in qualitatively the same manner at low and high masses (cf. Shimajiri et al. 2019a) and that the prestellar core mass function may be partly inherited from the distribution of filament line masses (André et al. 2019). The validity and details of this filament scenario for star formation and the initial mass function are actively debated, however (see, e.g., Gong & Ostriker 2015). But beyond ongoing debates, there is little doubt after the *Herschel* results that dense filaments are representative of the initial conditions of the bulk of star formation in molecular clouds. Characterizing the fragmentation mechanism of molecular filaments and their detailed density and velocity structure is thus crucial to our understanding of the star formation process.

Here, in an effort to clarify how prestellar cores form and grow within filaments, we present a detailed fragmentation study of the intermediate-mass filament NGC 2024S in Orion B, which has a line mass M_{line} of $\sim 62 \pm 13 M_\odot \text{pc}^{-1}$. This line

mass exceeds the thermally critical line mass $\sim 16 M_\odot \text{pc}^{-1}$ of an isothermal filament at ~ 10 K, suggesting that the NGC 2024S filament may not be in radial equilibrium. If this is the case, radial perturbations are expected to grow faster than perturbations along the filament axis, implying that the filament may not be able to fragment into prestellar cores before radially contracting to a spindle (e.g., Inutsuka & Miyama 1992, 1997). However, magnetohydrodynamics turbulence and/or static magnetic fields can increase the effective critical line mass (Fiege & Pudritz 2000; Jackson et al. 2010; Tomisaka 2014; Kashiwagi & Tomisaka 2021; Pattle et al. 2022). Accordingly, radial support provided by magnetohydrodynamics waves and/or magnetic fields may stabilize the filament and allow it to fragment along its length.

The NGC 2024 region is located in the southern part of the Orion B molecular cloud ($d = 400$ pc, Gibb 2008) and is known to be a very active site of star formation, with an estimated star formation rate of $9.2\text{--}13.8 \times 10^{-6} M_\odot \text{yr}^{-1}$ (Shimajiri et al. 2017). Using *Herschel* Gould Belt Survey (HGBS) data, Könyves et al. (2020) found that 60–90% of prestellar cores are closely associated with filaments in Orion B and observed that the most massive prestellar cores are spatially segregated in the highest column density areas. Orion B including the NGC 2024 region was also observed as part of the ORION-B (Outstanding Radio Imaging of Orion B) large program with the IRAM 30m telescope in 15 molecular lines, including ^{12}CO (1–0), ^{13}CO (1–0), C^{18}O (1–0), and H^{13}CO^+ (1–0) with a velocity resolution of $\sim 0.5 \text{ km s}^{-1}$ by Pety et al. (2017). The authors reported that 54.5%, 39.4%, 23.5%, and 7.8% of the total line fluxes in ^{12}CO (1–0), ^{13}CO (1–0), C^{18}O (1–0), and H^{13}CO^+ (1–0), respectively, are from the $A_V = 1\text{--}6$ area, while 45.6%, 60%, 78%, and 90% of the same line fluxes are from the $A_V = 6\text{--}222$ area in Orion B. Based on the ORION-B C^{18}O (1–0) data, Orkisz et al. (2019) find an average filament width of $\sim 0.12 \pm 0.04$ pc, consistent with the typical filament width found from *Herschel* column density data (e.g., Arzoumanian et al. 2019). Recently, the presence of a cloud-cloud collision in this region was suggested by NANTEN2 ^{13}CO (2–1) observations (Enokiya et al. 2021).

To investigate how molecular filaments fragment into cores, we performed observations of NGC 2024 with both the Nobeyama 45m telescope and the Northern Extended Millimeter Array (NOEMA) interferometer. In this paper, we focus on the southwestern part of NGC 2024, NGC 2024S, to avoid the effect of the H_{II} region located in the northern part. The paper is organized as follows: In Sect. 2 we describe our Nobeyama 45m and NOEMA observations. In Sect. 3, we present the results of ^{12}CO (1–0), ^{13}CO (1–0), C^{18}O (1–0), and H^{13}CO^+ (1–0) mappings toward the Orion B/NGC 2024 region. In Sect. 4, we discuss whether the cores are formed via the fragmentation of the filament. In Sect. 5, we summarize our results.

2. Observations and data

2.1. HGBS and ArT&MiS+Herschel column density maps

We used the *Herschel* H_2 column density map constructed from HGBS data by Könyves et al. (2020), publicly available². The effective resolution of this column density map is $18''.2$. Figure 1 shows the *Herschel* column density map toward the Orion B/NGC 2024 region.

the background emission is subtracted. The uncertainty comes from the uncertainty in the background subtraction.

² <http://gouldbelt-herschel.cea.fr/archives>

¹ The line mass was estimated by integrating over the filament area corresponding to $A_V > 8$ in the *Herschel* column density map where

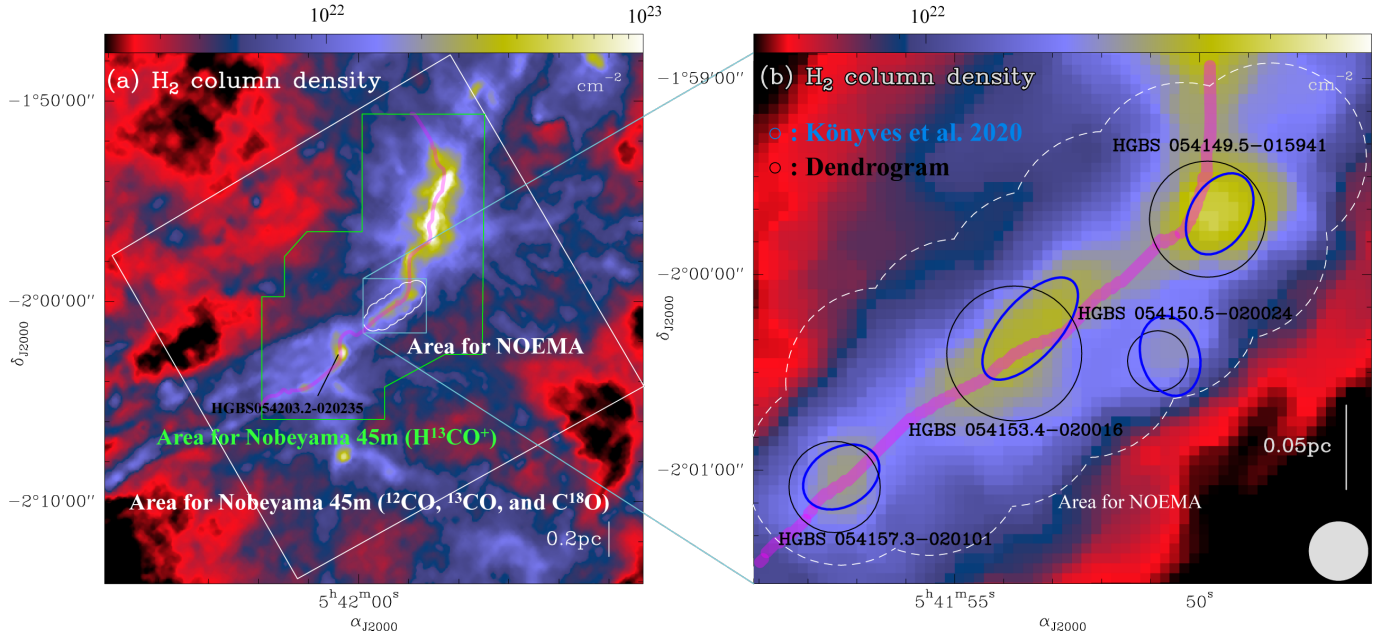


Fig. 1. *Herschel* column density map at an angular resolution of $18''.2$ toward the NGC 2024 region (a) and toward the area observed with the NOEMA interferometer (b). The *Herschel* column density map is from HGBS data (Könyves et al. 2020). In both panels, the magenta curve indicates the filament crest. The filament crest is determined by the DisPerSE algorithm (Sousbie 2011; Sousbie et al. 2011; Arzoumanian et al. 2011). In panel (a), the white box indicates the field observed in the ^{12}CO (1–0), ^{13}CO (1–0), and C^{18}O (1–0) lines with the Nobeyama 45m telescope. The green polygon outlines the field observed in H^{13}CO^+ (1–0). The dashed white circles indicate the field of view of the NOEMA mosaic observations. In panel (b), the blue open ellipses mark the cores identified by Könyves et al. (2020) and the black open circles the cores identified in the *Herschel* map via the dendrogram analysis. The sizes of the ellipses and circles reflect the core sizes estimated by Könyves et al. (2020) and from the dendrogram analysis, respectively.

We also produced a higher resolution column density map by combining the *Herschel* data with ArTéMiS³ data following the approach described in Schuller et al. (2021). Hereafter, we call this map the ArTéMiS+*Herschel* column density map. The details of the Orion B/NGC 2024 ArTéMiS observations, similar to the Orion A observations presented by Schuller et al. (2021) will be given in a separate paper.

2.2. Nobeyama 45m observations

Between 27 February 2017 and 1 March 2017, we carried out mapping observations in ^{12}CO (1–0, 115.2701204 GHz), ^{13}CO (1–0, 110.201354 GHz), C^{18}O (1–0, 109.782176 GHz), and H^{13}CO^+ (86.75433 GHz) toward the NGC 2024 region in the Orion B molecular cloud with the FOREST receiver installed on the Nobeyama 45m telescope. The ^{12}CO (1–0), ^{13}CO (1–0), and C^{18}O (1–0) lines were observed simultaneously. At 115 GHz, the telescope has a beam size of $15''.1$ (half-power beam width, HPBW). As the backend, we used the spectrometer, Spectral Analysis Machine for the 45m telescope (SAM45), which has a 31 MHz bandwidth and a frequency resolution of 7.63 kHz. The frequency resolution corresponds to a velocity resolution of $\sim 0.02 \text{ km s}^{-1}$ at 115 GHz. The standard chopper wheel method was used to convert the observed signal to the antenna temperature T_A^* in units of K, corrected for the atmospheric attenuation. To calibrate the intensity scale for the CO (and isotopes), we observed FIR 4 in OMC-2 with a small box of $2' \times 2'$ and a center of $(\text{RA}_{\text{J2000}}, \text{Dec}_{\text{J2000}}) = (5^{\text{h}}35^{\text{m}}26^{\text{s}}.8, -5^{\circ}9^{\text{m}}57^{\text{s}}.4)$. By direct

³ See <https://www.apex-telescope.org/ns/artemis/> ArTéMiS stands for “ARchitectures de bolomètres pour des TELEscopes à grand champ de vue dans le domaine sub-Millimétrique au Sol” in French.

comparison between the obtained data and the data obtained in Shimajiri et al. (2011, 2014, 2017), we obtained the intensity scaling factors from T_A^* to T_{MB} for each line. The estimated intensity scaling factors are applied to all of the data. Thus, the intensities of the data in this paper are in T_{MB} . The telescope pointing was checked every hour by observing the SiO maser sources, Ori-KL, and was better than $3''$ throughout the entire observation. Our mapping observations were made with the mapping technique. We chose the position of $(\text{RA}_{\text{J2000}}, \text{Dec}_{\text{J2000}}) = (5^{\text{h}}49^{\text{m}}45^{\text{s}}.115, -1^{\circ}56^{\text{m}}8^{\text{s}}.54)$ as the off position. We obtained on-the-fly maps with two different scanning directions along the RA or Dec axes covering the $20' \times 20'$ for CO and its isotopes and $5' \times 6'$ for H^{13}CO^+ and combined them into a single map to reduce the scanning effects as much as possible. As a convolution function, we applied a spherical function with a full width at half maximum (FWHM) of half of the beam size, resulting in an effective beam size of $21''.6$ for CO and $25''$ for H^{13}CO^+ . In order to improve the sensitivity, we combined the H^{13}CO^+ data with the data obtained in Shimajiri et al. (2017). We smoothed the data with a Gaussian function resulting in a final effective beam size of $25''$ for CO and its isotope and $30''$ for H^{13}CO^+ . The 1σ noise level of the final data with an effective resolution of $25''$ is 0.57 K, 0.30 K, 0.30 K in T_{MB} for ^{12}CO (1–0), ^{13}CO (1–0), and C^{18}O (1–0) at a velocity resolution of 0.1 km s^{-1} (Table 1). The 1σ noise level with an effective resolution of $30''$ is 0.13 K in T_{MB} for H^{13}CO^+ (1–0) at a velocity resolution of 0.1 km s^{-1} (Table 1).

2.3. NOEMA observations

We carried out millimeter interferometric 12-pointing mosaic observations of the NGC 2024 region in the H^{13}CO^+ (1–0)

Table 1. Nobeyama 45m observations.

Molecule	^{12}CO	^{13}CO	C^{18}O	H^{13}CO^+
Transition	(1–0)	(1–0)	(1–0)	(1–0)
Frequency	115.2701204 GHz	110.201354 GHz	109.782176 GHz	86.75433 GHz
Telescope	Nobeyama 45m			
Receiver	FOREST	FOREST	FOREST	TZ ^(†) FOREST
Spectrometer	SAM45			
Obs. period	28 Feb.–1 March 2017			7–21 May 2015 ^(†) 27 Feb. 2017
θ_{eff}	25''	25''	25''	30''
	~0.05 pc	~0.05 pc	~0.05 pc	~0.06 pc
dV	0.1 km s ⁻¹	0.1 km s ⁻¹	0.1 km s ⁻¹	0.1 km s ⁻¹
rms	0.57 K	0.30 K	0.30 K	0.13 K

Notes. ^(†) The data were taken from [Shimajiri et al. \(2017\)](#).

Table 2. NOEMA observations.

Configuration	D
Baseline	4.5–37.0 k λ
Primary beam HPBW	58' 1~0.11 pc
Synthesized Beam HPBW	6' 40 \times 3' 68 (PA: -186.18°)
	0.012 pc \times 0.007 pc
Velocity resolution	0.13 km s ⁻¹
Gain calibrators	0458–020, 0550+032
Bandpass calibrator	3C84
Rms noise level	16 mJy beam ⁻¹

line at 86.75433 GHz with NOEMA in the D configuration during a period from 9 August 2016 to 1 September 2017. The data were obtained with the narrow-band correlator that was configured with 512 channels per baseline and a bandwidth of 20 MHz. The channel spacing is 39 kHz which corresponds to 0.13 km s⁻¹ at 86 GHz. Table 2 summarizes the parameters for the line observations. Using CLIC which is part of the GILDAS software, calibration was carried out following standard procedures. We adopted natural weighting for the imaging of the H¹³CO⁺ emission. Since the minimum projected baseline length of the H¹³CO⁺ observations was 4.5 k λ , the NOEMA data are insensitive to structures more extended than 36' 7 (0.07 pc) at the 10% level ([Wilner & Welch 1994](#)).

2.4. Combining NOEMA and 45m H¹³CO⁺ data

In order to produce a data set with both information on extended emission and high angular resolution, we re-gridded the Nobeyama H¹³CO⁺(1–0) data to NOEMA H¹³CO⁺(1–0) data both in velocity and position using the task “regrid” and combined the NOEMA and Nobeyama H¹³CO⁺(1–0) observations using the task “immerge” in the Miriad software package ([Sault et al. 1995](#)). A calibration factor of 1.0 was applied to the NOEMA H¹³CO⁺(1–0) data.

Figure A.2 compares the velocity channel maps of (i) the NOEMA H¹³CO⁺(1–0) data, (ii) the Nobeyama H¹³CO⁺(1–0) data, (iii) the combined NOEMA + Nobeyama data (hereafter, called NOEMA+45m data), and (iv) the NOEMA+45m data smoothed to the angular resolution of the Nobeyama H¹³CO⁺(1–0) data (hereafter, called the smoothed NOEMA+45m data).

It can be seen in each channel map that extended emission has been restored in the NOEMA+45m data compared to the NOEMA-only data. In addition, the smoothed NOEMA+45m data cube is very similar to the Nobeyama data cube: The intensity in the smoothed NOEMA+45m data is consistent to within 10% with that in the Nobeyama data. The rms noise level of the NOEMA+45m data at a velocity resolution of 0.13 km s⁻¹ is 0.017 Jy beam⁻¹.

3. Results and analysis

3.1. Spatial distribution of ^{12}CO (1–0), ^{13}CO (1–0), C^{18}O (1–0), and H^{13}CO^+ (1–0) emission

3.1.1. ^{12}CO (1–0), ^{13}CO (1–0), and C^{18}O (1–0) emission

Figure 2 shows the velocity integrated intensity maps observed in the ^{12}CO (1–0), ^{13}CO (1–0), and C^{18}O (1–0) lines at the Nobeyama 45m telescope. In the maps for $1.5 < V_{\text{LSR}} < 7.8$ km s⁻¹ (Figs. 2a, f, and k), faint ^{12}CO (1–0) and ^{13}CO (1–0) emission can be seen. In the maps for $7.9 < V_{\text{LSR}} < 9.8$ km s⁻¹ (Figs. 2b, g, and l), strong ^{13}CO (1–0) and C^{18}O (1–0) emission is associated with the main peak in the *Herschel* column density map. Furthermore, the ^{12}CO (1–0) and ^{13}CO (1–0) emission is stronger in the northern part of the field. In the maps for $9.9 < V_{\text{LSR}} < 11.6$ km s⁻¹ (Figs. 2c, h, and m), the ^{13}CO (1–0) and C^{18}O (1–0) emission is seen toward the filament traced in the *Herschel* column density map of Fig. 1. In the maps for $11.7 < V_{\text{LSR}} < 14.3$ km s⁻¹ (Figs. 2d, i, and n), the emission detected in ^{12}CO (1–0), ^{13}CO (1–0), and C^{18}O (1–0) is distributed mostly in the southern part of the field. In the maps for $14.4 < V_{\text{LSR}} < 14.8$ km s⁻¹ (Figs. 2e, j, and o), significant emission can be seen only in ^{12}CO . Figure 3 shows a three-color composite image with the *Herschel* H₂ column density map (in green) and the blueshifted and redshifted ^{13}CO emission detected by the Nobeyama telescope. The blueshifted emission lies to the northeast of the filament, while the redshifted emission lies to the southwest of it.

3.1.2. H¹³CO⁺(1–0) emission

[Shimajiri et al. \(2017\)](#) found that the spatial distribution of H¹³CO⁺(1–0) emission in NGC 2024 is similar to that seen in dust emission in the *Herschel* column density maps of the

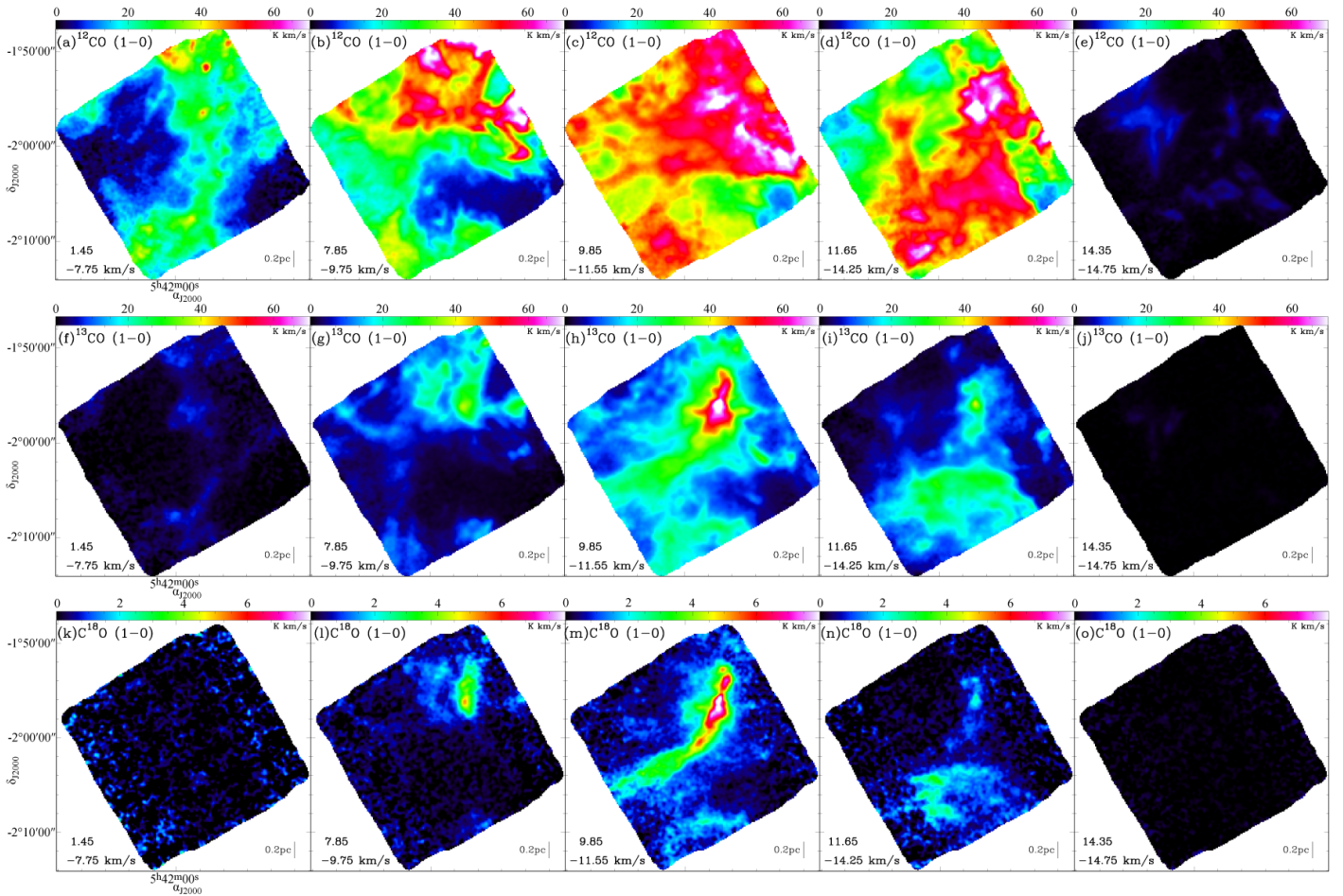


Fig. 2. (a–e) ^{12}CO (1–0), (f–j) ^{13}CO (1–0), and (k–o) C^{18}O (1–0) maps integrated in the velocity ranges 1.45–7.75 km s $^{-1}$, 7.85–9.75 km s $^{-1}$, 9.85–11.55 km s $^{-1}$, 11.65–14.25 km s $^{-1}$, and 14.35–14.75 km s $^{-1}$. The integrated velocity range is indicated in the bottom-left corner of each panel. The coverage of these observations of CO and its isotope is also shown in Fig. 1.

Ophiuchus, Aquila, and Orion B clouds and that the optical depth of the $\text{H}^{13}\text{CO}^+(1-0)$ line in these clouds is low (see Table A.1 in Shimajiri et al. 2017). This suggests that the $\text{H}^{13}\text{CO}^+(1-0)$ line is a good tracer of the dense filaments detected with *Herschel* and is suitable to investigate their underlying velocity field.

Figure 4 shows the distribution of the H^{13}CO^+ (1–0) emission. The H^{13}CO^+ emission traces the dense part of the filament seen in the *Herschel* H_2 column density well (Figs. 1 and 4a), while the C^{18}O emission traces larger-scale structures in the *Herschel* H_2 column density map (Figs. 1 and 2m; see also Fig. A.3). At the core scale, the H^{13}CO^+ emission traces well the cores detected in the *Herschel* H_2 column density map (see Sect. 3.1.4), while the C^{18}O emission does not trace some of the *Herschel* cores. This is likely due to the depletion of CO molecules onto grains at high density (e.g., Tafalla et al. 2004). A similar result that H^{13}CO^+ emission traces dense dusty cores better than C^{18}O emission was also reported in the Orion A molecular cloud ($d = 400$ pc, Shimajiri et al. 2015). The correlation between H^{13}CO^+ and *Herschel* H_2 data has a smaller scatter than that between C^{18}O and *Herschel* H_2 , confirming that the H^{13}CO^+ emission traces well the dense structures seen in the *Herschel* H_2 column density map (Fig. A.4). Thus, the H^{13}CO^+ emission provides a better probe of the velocity and density structure of the cores and filaments seen in the *Herschel* H_2 column density map than C^{18}O .

3.1.3. Gas distribution in the NOEMA high-spatial-resolution maps

Panel c of Fig. 4 shows the integrated intensity map of the H^{13}CO^+ (1–0) emission observed with NOEMA. The overall distribution of the NOEMA H^{13}CO^+ (1–0) emission is consistent with that seen in both the Nobeyama H^{13}CO^+ (1–0) map and the *Herschel* column density map. In the western part of the NOEMA map (RA_{2000} , $\text{Dec}_{2000} = \sim 5^{\text{h}}41^{\text{m}}50^{\text{s}}$, $\sim -2^{\circ}0^{\text{m}}25^{\text{s}}$), a secondary structure can be seen. This structure can also be recognized in the *Herschel* column density map and in the Nobeyama H^{13}CO^+ (1–0) velocity channel maps at $10.7 < V_{\text{LSR}} < 11.0$ km s $^{-1}$ (Fig. 5).

3.1.4. Core identification in the NOEMA+45m H^{13}CO^+ data cube

Könyves et al. (2020) obtained a census of dense cores in Orion B from the *Herschel* data using the *getsources* algorithm (Men'shchikov et al. 2012). In the field mapped here with NOEMA, four cores were identified.

Here, we identified cores in the NOEMA+45m H^{13}CO^+ data cube to compare core spacing and filament width. As *getsources* cannot be used with spectral line data, we performed a dendrogram analysis using the *astrodendro* package⁴

⁴ <http://www.dendrograms.org>

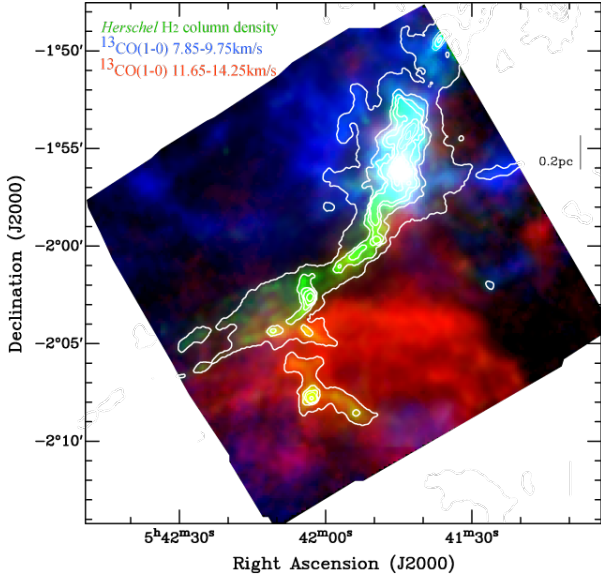


Fig. 3. Three-color composite image of the *Herschel* H₂ column density map (green) and the blueshifted and redshifted Nobeyama ¹³CO emission (red: 7.85–9.75 km s⁻¹ and blue: 11.65–14.25 km s⁻¹; see also Figs. 2g and i). The white contours correspond to A_V levels of 8, 16, 24, 32, 64, 128, and 256 mag (assuming N_{H₂}/A_V = 0.94 × 10²¹ cm⁻²; Bohlin et al. 1978) in the *Herschel* H₂ column density map at an angular resolution of 18''.2.

(Rosolowsky et al. 2008). When a data set is sensitive to a whole hierarchy of structures such as clumps, filaments, and cores, the dendrogram algorithm is a powerful technique to trace this hierarchy (cf. Friesen et al. 2016). In addition, we also extracted cores in the *Herschel* column density map using the same dendrogram technique for comparison with both the cores identified here in the NOEMA+45m H¹³CO⁺ data cube and the cores identified by Könyves et al. (2020) with getsources in the *Herschel* data.

To perform a dendrogram analysis, three input parameters are required. The first one, min_value, is the starting level, that is, the minimum intensity value below each extracted structure. The second one, min_delta, is a step and corresponds to the minimum height of each extracted structure above the starting level. The third one, min_npix, is the minimum number of pixels that a significant structure must contain. The detected structures are categorized into three types, trunk, branch, and leaf, following their hierarchy (see Rosolowsky et al. 2008). In this paper, we refer to the smallest, leaf structures as candidate cores and focus on the detection of such cores.

To identify cores in the NOEMA+45m H¹³CO⁺ (1–0) data cube, we applied the dendrogram algorithm with min_value=4σ, min_delta=4σ, and min_npix=14.9 pixels (=A_{beam}/A_{pixel}, where A_{beam} and A_{pixel} are the surface area of the beam and pixel). We note that min_npix is the total number of pixels where the structure is detected overall velocity channels. Here, we used the signal-to-noise ratio map to avoid the detection of spurious sources due to a nonuniform noise distribution. After performing a dendrogram analysis with these parameters, we rejected ambiguous or fake core candidates that do not have min_npix pixels in two or more contiguous velocity channels.

To identify dendrogram cores in the *Herschel* column density map, we applied the algorithm with A_V = 8⁵ (assuming

⁵ Here, we focus on the identification of cores in the NGC 2024S filament. Prestellar cores are typically found in filaments with A_V values above 8 in *Herschel* data (Könyves et al. 2015). Thus, we adopted A_V = 8 for min_value.

N_{H₂}/A_V = 0.94 × 10²¹ cm⁻², Bohlin et al. 1978) for the min_value, A_V = 1 for min_delta, and 28.9 pixels (=A_{beam}/A_{pixel}) for min_npix.

In this way, we identified twelve cores in the NOEMA+45m H¹³CO⁺ data cube. We also extracted four cores in the portion of the *Herschel* column density map covered by NOEMA (which has an effective resolution θ_{beam} = 18''.2 ~ 0.04 pc; see Fig. 4a). The positions of the cores identified here are consistent with those found in the *Herschel* data by Könyves et al. (2020). As can be seen in Fig. 4c, each core detected in the *Herschel* map corresponds to a single core in the NOEMA+45m H¹³CO⁺ data, suggesting that the *Herschel* cores do not have significant substructure at a scale of ~5'' (~0.01 pc or 2000 au). The positions of the cores identified in the *Herschel* and NOEMA+45m data are listed in Tables 3 and 4, respectively.

The mass of each dendrogram core was estimated as

$$M_{\text{core}}^{\text{Dendro}} [M_{\odot}] = N(\text{H}_2) m_{\text{H}} \mu_{\text{H}_2} A_{\text{core}}^{\text{Dendro}}, \quad (1)$$

where m_H is the hydrogen atom mass, μ_{H₂} = 2.8 is the mean molecular weight per H₂ molecule, and A_{core}^{Dendro} is the projected area of each core identified by the dendrogram analysis. Here, the total N(H₂) was measured using the Bijection scheme as defined by Rosolowsky et al. (2008). The uncertainty in M_{core}^{Dendro} is typically a factor of 2, mainly due to uncertainties in the dust opacity (cf. Roy et al. 2014). The core masses from the dendrogram analysis range from 0.44 M_⊙ to 2.84 M_⊙, with a mean value <M_{core}^{Dendro}> = 1.7 ± 1.0 M_⊙. The core masses reported by Könyves et al. (2020) have a mean value <M_{core}^{Herschel}> = 2.5 ± 1.2 M_⊙ (see also Table 3) and are consistent within better than a factor of ~2 with the masses from the dendrogram analysis. The main reason why the two sets of mass estimates differ slightly is that the dendrogram technique does not subtract background emission and returns different source sizes.

Under the assumption that each core has a spheroidal shape and a density profile of ρ ∝ r⁻², we also estimated the virial masses M_{VIR}^{Herschel} and M_{VIR}^{Dendro} of the detected cores as follows (see Ikeda et al. 2007; Shimajiri et al. 2015),

$$M_{\text{VIR}}^{\text{Herschel}} [M_{\odot}] = \frac{3R_{\text{core}}^{\text{Herschel}} \sigma_{\text{Herschel}}^2}{G} = 125 R_{\text{core}}^{\text{Herschel}} \left(dV_{\text{H}^{13}\text{CO}^+, \text{FWHM}}^{\text{Herschel}} \right)^2$$

or

$$M_{\text{VIR}}^{\text{Dendro}} [M_{\odot}] = \frac{3R_{\text{core}}^{\text{Dendro}} \sigma_{\text{Dendro}}^2}{G} = 125 R_{\text{core}}^{\text{Dendro}} \left(dV_{\text{H}^{13}\text{CO}^+, \text{FWHM}}^{\text{Dendro}} \right)^2. \quad (3)$$

The radius R_{core}^{Herschel} is provided in Könyves et al. (2020). The radius R_{core}^{Dendro} of each core was estimated as R_{core}^{Dendro} [pc] = √(A_{core}^{Dendro}/π). The velocity dispersion σ_{Herschel} and σ_{Dendro} was determined as σ_{Herschel} = dV_{H¹³CO⁺,FWHM}^Herschel / √(8 ln 2) and σ_{Dendro} = dV_{H¹³CO⁺,FWHM}^Dendro / √(8 ln 2), where dV_{H¹³CO⁺,FWHM}^Dendro is the mean FWHM velocity width of the Nobeyama+45m H¹³CO⁺(1–0) emission among pixels in A_{core}^{Dendro} and dV_{H¹³CO⁺,FWHM}^Herschel is the mean FWHM velocity width of the Nobeyama+45m H¹³CO⁺(1–0) emission among the area within 1 R_{core}^{Herschel} from the core position (RA_{J2000}, Dec_{J2000}). The mean FWHM velocity width among cores ranges from 0.4 km s⁻¹ to 0.7 km s⁻¹, while the typical FWHM velocity along the filamentary structure is 0.6 km s⁻¹. The virial mass ratios α_{VIR}^{Herschel} (≡ M_{VIR}^{Herschel}/M_{core}^{Herschel}) and α_{VIR}^{Dendro} (≡ M_{VIR}^{Dendro}/M_{core}^{Dendro}) are lower than ~2, suggesting that all four cores are gravitationally bound. The derived physical parameters of each core are given in Table 3.}}}}

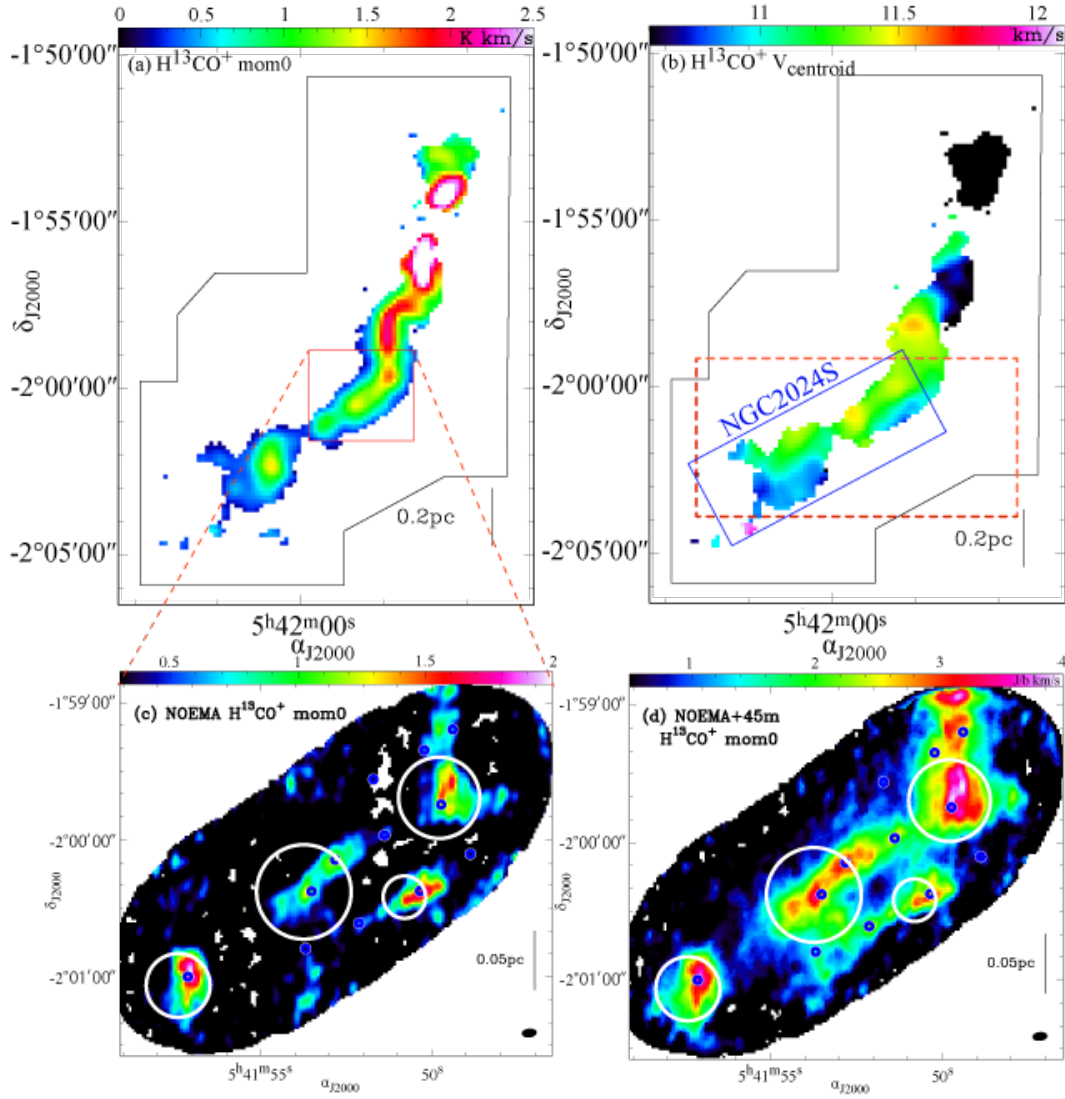


Fig. 4. (a) Nobeyama 45m H^{13}CO^+ (1–0) integrated intensity, (b) H^{13}CO^+ (1–0) centroid velocity map, (c) NOEMA, and (d) NOEMA+45m H^{13}CO^+ (1–0) integrated intensity maps. The integrated velocity range is from 10.21 km s^{-1} to 11.96 km s^{-1} . In panels a and b, black polygons outline the field observed in the H^{13}CO^+ (1–0) line. In panel a, the red box indicates the area shown in panels c and d. In panel b, the dashed red box indicates the area shown in Fig. 7. The white open circles in panels c and d indicate the positions of the cores identified in the *Herschel* map via the dendrogram analysis. The sizes of the white open circles reflect the *Herschel* source sizes. The small blue open circles in panels c and d mark the positions of the cores identified in the NOEMA H^{13}CO^+ map via the dendrogram analysis with a fixed symbol size. The filled circles at the bottom right indicate the beam sizes in panels a and b. See also Fig. A.1.

3.1.5. Filament properties

Figure 6 shows, in log-log format, the median radial column density profiles measured on the northeastern and southwestern sides of the NGC 2024S filament in the $8''$ -resolution ArTéMiS+*Herschel* data whose background emission is not subtracted. Here, the filament crest was defined using the DisPerSE algorithm (Sousbie 2011; Sousbie et al. 2011; Arzoumanian et al. 2011). Following Arzoumanian et al. (2011) and Palmeirim et al. (2013), we fitted the density profiles on the northeastern and southwestern sides of the NGC 2024S filament with a Plummer-like model as below:

$$N_{\text{H}_2}(r) = \frac{N_{\text{H}_2}^0}{\left[1 + (r/R_{\text{flat}})^2\right]^{\frac{p-1}{2}}} + B_{\text{kg}}, \quad (4)$$

where $N_{\text{H}_2}^0$ is the column density at filament center, R_{flat} is the radius of the flat inner region, p is the power-law exponent at

larger radii, and B_{kg} is the column density of the background. $N_{\text{H}_2}^0$ is expressed as $A_p \rho_c R_{\text{flat}} / \mu m_{\text{H}}$ where $A_p = \frac{1}{\cos i} \times B\left(\frac{1}{2}, \frac{p-1}{2}\right)$ is a finite constant factor. The factor $\frac{1}{\cos i}$ takes into account the inclination of the filament to the plane of the sky. Here, we assumed $i=0$. For a population of randomly oriented filaments with respect to the plane of the sky, the net effect is a factor of $\langle \frac{1}{\cos i} \rangle \sim 1.57$ on average (cf. Arzoumanian et al. 2011). $B\left(\frac{1}{2}, \frac{p-1}{2}\right)$ is the Euler beta function. The fitting results are summarized in Table 5. The density at the center of the filament is estimated to be $n_c = (1.2 \pm 0.4) \times 10^5 \text{ cm}^{-3}$ from the Plummer fits to the radial profile averaged between the southwestern and northeastern sides of the filament.

The half-power diameter of the filament as derived from Plummer fitting, $D_{\text{HP}}^{\text{Plummer}}$, corresponds to:

$$D_{\text{HP}}^{\text{Plummer}} = \sqrt{2^{\frac{2}{p-1}} - 1} \times D_{\text{flat}}, \quad (5)$$

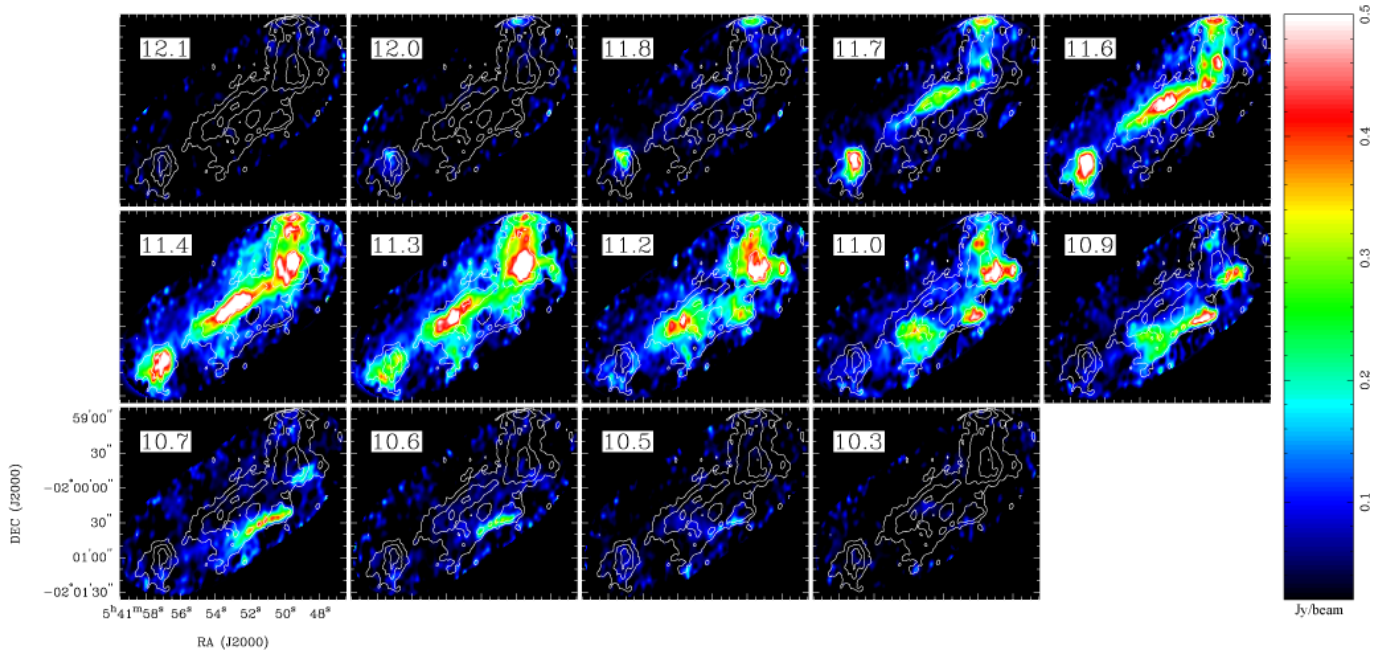


Fig. 5. Velocity channel maps of NOEMA+45m H^{13}CO^+ (1–0) emission. Contours indicate NOEMA+45m H^{13}CO^+ (1–0) integrated intensity map and the contour levels of these maps start at 0.1 Jy beam^{-1} levels with an interval of 0.1 Jy beam^{-1} .

Table 3. *Herschel* cores identified by Dendrogram.

Core name	HGBS 054157.3-020101	HGBS 054153.4-020016	HGBS 054150.5-020024	HGBS 054149.5-015941
Core type ⁽⁺⁾	Prestellar	Prestellar	Prestellar	Class-0/I ⁽⁺⁺⁾
$\text{RA}_{\text{J2000}}^{\text{Herschel}}$ (**)	$05^{\text{h}}41^{\text{m}}57^{\text{s}}.3$	$05^{\text{h}}41^{\text{m}}53^{\text{s}}.5$	$05^{\text{h}}41^{\text{m}}50^{\text{s}}.6$	$05^{\text{h}}41^{\text{m}}49^{\text{s}}.6$
$\text{Dec}_{\text{J2000}}^{\text{Herschel}}$ (**)	$-02^{\circ}01^{\text{m}}01^{\text{s}}.9$	$-02^{\circ}00^{\text{m}}16^{\text{s}}.4$	$-02^{\circ}00^{\text{m}}24^{\text{s}}.7$	$-01^{\circ}59^{\text{m}}41^{\text{s}}.2$
$R_{\text{core}}^{\text{Herschel}}$ (pc)	0.024	0.034	0.025	0.026
$M_{\text{core}}^{\text{Herschel}}$ (M_{\odot})	1.63	3.80	0.99	3.59
$dV_{\text{H}^{13}\text{CO}^+, \text{FWHM}}^{\text{Herschel}}$ (km s^{-1})	0.51	0.56	0.73	0.61
$V_{\text{H}^{13}\text{CO}^+, \text{sys}}^{\text{Herschel}}$ (km s^{-1})	11.44	11.31	10.80	11.36
$M_{\text{VIR}}^{\text{Herschel}}$ (M_{\odot})	0.79	1.35	1.68	1.19
$\alpha_{\text{VIR}}^{\text{Herschel}}$ (*)	0.5	0.4	1.7	0.3
$\text{RA}_{\text{J2000}}^{\text{Dendro}}$ (**)	$05^{\text{h}}41^{\text{m}}57^{\text{s}}.4$	$05^{\text{h}}41^{\text{m}}53^{\text{s}}.7$	$05^{\text{h}}41^{\text{m}}50^{\text{s}}.8$	$05^{\text{h}}41^{\text{m}}49^{\text{s}}.8$
$\text{Dec}_{\text{J2000}}^{\text{Dendro}}$ (**)	$-02^{\circ}01^{\text{m}}03^{\text{s}}.8$	$-02^{\circ}00^{\text{m}}22^{\text{s}}.9$	$-02^{\circ}00^{\text{m}}25^{\text{s}}.2$	$-01^{\circ}59^{\text{m}}41^{\text{s}}.7$
$R_{\text{core}}^{\text{Dendro}}$ (pc)	0.027	0.040	0.018	0.035
$M_{\text{core}}^{\text{Dendro}}$ (M_{\odot})	1.07	2.84	0.44	2.50
$dV_{\text{H}^{13}\text{CO}^+, \text{FWHM}}^{\text{Dendro}}$ (km s^{-1})	0.44	0.60	0.68	0.63
$V_{\text{H}^{13}\text{CO}^+, \text{sys}}^{\text{Dendro}}$ (km s^{-1})	11.48	11.37	11.09	11.33
$M_{\text{VIR}}^{\text{Dendro}}$ (M_{\odot})	0.66	1.81	1.03	1.72
$\alpha_{\text{VIR}}^{\text{Dendro}}$ (*)	0.6	0.6	2.3	0.7

Notes. (**) $\text{RA}_{\text{J2000}}^{\text{Herschel}}$ and $\text{Dec}_{\text{J2000}}^{\text{Herschel}}$ are the positions of cores identified by Könyves et al. (2020). $\text{RA}_{\text{J2000}}^{\text{Dendro}}$ and $\text{Dec}_{\text{J2000}}^{\text{Dendro}}$ are the positions of cores identified by Dendrogram. (\dagger) $dV_{\text{H}^{13}\text{CO}^+, \text{FWHM}}^{\text{Herschel}}$, $V_{\text{H}^{13}\text{CO}^+, \text{sys}}^{\text{Herschel}}$, $dV_{\text{H}^{13}\text{CO}^+, \text{FWHM}}^{\text{Dendro}}$, and $V_{\text{H}^{13}\text{CO}^+, \text{sys}}^{\text{Dendro}}$ are measured from the NOEMA+45m H^{13}CO^+ (1–0) map. $dV_{\text{H}^{13}\text{CO}^+, \text{FWHM}}^{\text{Herschel}}$ are measured from the spectrum averaged toward the area with a center of $\text{RA}_{\text{J2000}}^{\text{Herschel}}$ and $\text{Dec}_{\text{J2000}}^{\text{Herschel}}$ and a radius of $R_{\text{core}}^{\text{Herschel}}$ from the NOEMA+45m H^{13}CO^+ (1–0) map. $dV_{\text{H}^{13}\text{CO}^+, \text{FWHM}}^{\text{Dendro}}$ are measured from the spectrum averaged toward the area identified as the corresponding structure from the Nobeyama+45m H^{13}CO^+ (1–0) map. (\ddagger) $M_{\text{VIR}}^{\text{Herschel}} = 125 R_{\text{core}}^{\text{Herschel}} (dV_{\text{H}^{13}\text{CO}^+, \text{FWHM}}^{\text{Herschel}})^2$ and $M_{\text{VIR}}^{\text{Dendro}} = 125 R_{\text{core}}^{\text{Dendro}} (dV_{\text{H}^{13}\text{CO}^+, \text{FWHM}}^{\text{Dendro}})^2$. (*) $\alpha_{\text{VIR}}^{\text{Dendro}} = M_{\text{VIR}}^{\text{Dendro}} / M_{\text{core}}^{\text{Dendro}}$ and $\alpha_{\text{VIR}}^{\text{Herschel}} = M_{\text{VIR}}^{\text{Herschel}} / M_{\text{core}}^{\text{Herschel}}$. (+) From Könyves et al. (2020). (++) This object is identified as Class-0/I object [MGM]2882 by Megeath et al. (2012), while it is identified as prestellar core in Könyves et al. (2020). The separation between HGBS 054149.5-015941 and [MGM]2882 is $7''.2$ which is larger than the threshold of $6''$ of the cross-matching adopted in Könyves et al. (2020).

where $D_{\text{flat}} \equiv 2 \times R_{\text{flat}}$. $D_{\text{HP}}^{\text{Plummer}}$ provides a more robust measurement of the inner width of a Plummer-like profile than D_{flat} since its derivation is not as strongly correlated to that of p (cf.

Schuller et al. 2021). The half-power diameter $D_{\text{HP}}^{\text{Plummer}}$ of the NGC 2024S filament as derived from fitting the northeastern and southwestern sides of the median radial profile simultaneously

Table 4. H¹³CO⁺ cores identified by Dendrogram in the NOEMA+45m data cube.

ID	RA _{J2000}	Dec _{J2000}	$R_{\text{core}}^{\text{NOEMA+45m}}$ (pc)	$V_{\text{sys}}^{\text{NOEMA+45m}}$ (km s ⁻¹)	$dV_{\text{FWHM}}^{\text{NOEMA+45m}}$ (km s ⁻¹)	$M_{\text{VIR}}^{\text{NOEMA+45m}} (\ddagger)$ (M_{\odot})
1	05 ^h 41 ^m 57 ^s .1	-02°01 ^m 00 ^s .0	0.020	11.53	0.51	0.63
2	05 ^h 41 ^m 51 ^s .4	-01°59 ^m 58 ^s .1	0.013	11.50	0.51	0.42
3	05 ^h 41 ^m 52 ^s .8	-02°00 ^m 08 ^s .7	0.010	11.45	0.45	0.26
4	05 ^h 41 ^m 51 ^s .7	-01°59 ^m 33 ^s .6	0.008	11.38	0.42	0.18
5	05 ^h 41 ^m 53 ^s .7	-02°00 ^m 47 ^s .7	0.007	11.11	0.74	0.51
6	05 ^h 41 ^m 53 ^s .5	-02°00 ^m 22 ^s .6	0.012	11.32	0.47	0.32
7	05 ^h 41 ^m 49 ^s .4	-01°59 ^m 11 ^s .7	0.008	11.32	0.64	0.42
8	05 ^h 41 ^m 49 ^s .7	-01°59 ^m 44 ^s .6	0.007	11.24	0.52	0.23
9	05 ^h 41 ^m 50 ^s .2	-01°59 ^m 20 ^s .8	0.006	11.18	0.66	0.32
10	05 ^h 41 ^m 50 ^s .3	-02°00 ^m 22 ^s .4	0.011	10.96	0.55	0.43
11	05 ^h 41 ^m 48 ^s .9	-02°00 ^m 06 ^s .3	0.008	11.03	0.57	0.30
12	05 ^h 41 ^m 52 ^s .1	-02°00 ^m 36 ^s .5	0.008	10.88	0.74	0.54

Notes. (\ddagger) $M_{\text{VIR}}^{\text{NOEMA+45m}} = 125 R_{\text{core}}^{\text{NOEMA+45m}} (dV_{\text{FWHM}}^{\text{NOEMA+45m}})^2$.

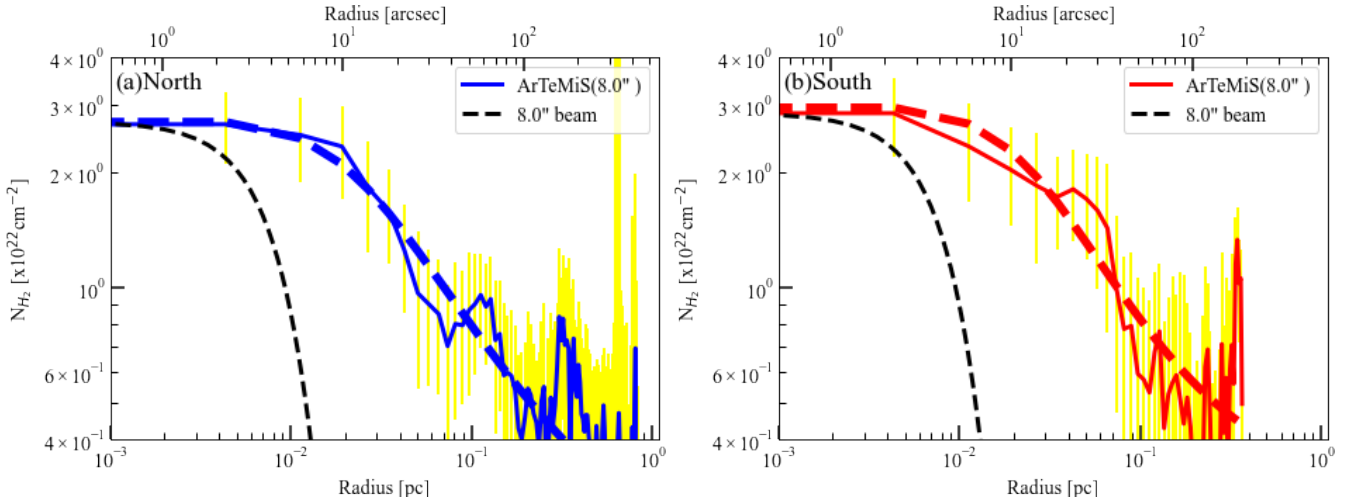


Fig. 6. Median radial ArTéMiS+*Herschel* column density profiles for the (a) northeastern and (b) southwestern side of the NGC 2024S filament. The defined crest of the filament is shown in Fig. B.1. The dashed black curves indicate the angular resolution of the ArTéMiS+*Herschel* column density map (8''). The dashed curves show the best-fit Plummer mode. The yellow bars show the dispersion ($\pm 1\sigma$) of the distribution of radial profiles along the filament. The area affected by the secondary component seen in the NOEMA H¹³CO⁺ data was avoided when producing the median radial profile for the southwestern side of the NGC 2024S filament (see Sect. 3.1.3).

is 0.081 ± 0.014 pc. (The $D_{\text{HP}}^{\text{Plummer}}$ values obtained by fitting the northeastern and southwestern sides of the radial profile separately are 0.078 ± 0.015 pc and 0.071 ± 0.040 pc, respectively).⁶ These values agree well with the half-power widths found in *Herschel* studies of Gould Belt filaments (Arzoumanian et al. 2011, 2019; Palmeirim et al. 2013).

We also estimate the virial mass of the filament, $M_{\text{line,vir}} \equiv 2 \sigma^2 / G \sim 84 \left(\frac{dV_{\text{FWHM}}}{\text{km s}^{-1}} \right)^2 [M_{\odot} \text{ pc}^{-1}]$ (Fiege & Pudritz 2000). The mean velocity width, dV_{FWHM} , is measured to be 0.62 km s^{-1} (min: 0.49 km s^{-1} , max: 0.84 km s^{-1}) from the Nobeyama H¹³CO⁺ (1–0) map. We note that the velocity width is measured toward the whole area mapped by the NOEMA. Thus, the virial mass of the NGC 2024S is $32.4 M_{\odot} \text{ pc}^{-1}$ (min: $20.2 M_{\odot} \text{ pc}^{-1}$, max: $59.0 M_{\odot} \text{ pc}^{-1}$).

⁶ Note that the p values differ slightly for each of the fit (see Table 5), which explains why the $D_{\text{HP}}^{\text{Plummer}}$ value from the two-sided fit is not a simple average of the two values obtained from the one-sided fits.

3.2. Velocity structure

The spectra in the Nobeyama C¹⁸O (1–0) and H¹³CO⁺ (1–0) data cubes show a single velocity component at all positions. Thus, we performed a Gaussian fitting analysis with a single component for all spectra. In this way, we obtained the centroid velocity at each pixel in the Nobeyama C¹⁸O (1–0) and H¹³CO⁺ (1–0) data. Figure 7 shows the C¹⁸O (1–0) and H¹³CO⁺ (1–0) centroid velocity maps. In the southeastern part of the dense elongated ridge corresponding to NGC 2024, a velocity gradient can be seen along the direction perpendicular to the filament. In the present paper, we refer to the southeastern part of the filamentary structure in NGC 2024, indicated by a red box in Fig. 4b, as the NGC 2024S filament. In this area, the blueshifted and redshifted H¹³CO⁺ velocity components are distributed on the southwestern and the northeastern side of the filament crest, respectively, indicating the presence of a transverse velocity gradient across the filament.

Table 5. Properties of the NGC 2024S filament.

Parameter	Northeastern side ^(†)	Southwestern side ^(†,*)	Averaged both sides	B211/B213 filament ^(‡)
(1)	(2)	(3)	(4)	(5).
$N_{\text{H}_2}^0$ ($\times 10^{21}$ cm ⁻²)	26.1 \pm 0.2	27.2 \pm 0.4	26.2 \pm 0.2	14.4 \pm 1.4
R_{flat} (pc)	0.019 \pm 0.005	0.021 \pm 0.011	0.021 \pm 0.005	0.032 \pm 0.014
p	1.8 \pm 0.2	2.0 \pm 0.6	1.9 \pm 0.2	2.0 \pm 0.09
$D_{\text{HP}}^{\text{Plummer}}$ (pc)	0.078 \pm 0.015	0.071 \pm 0.040	0.081 \pm 0.014 ^(*)	0.11 \pm 0.02
B_{kg} ($\times 10^{21}$ cm ⁻²)	1.58 \pm 0.07	2.98 \pm 2.42	1.56 \pm 0.01	0.67 \pm 0.17
n_c ($\times 10^5$ cm ⁻³)	1.2 \pm 0.5	1.4 \pm 0.1	1.2 \pm 0.4	0.45

Notes. ^(†) Fitting results on the 8'' resolution ArTéMiS+*Herschel* column density map. ^(*) The area affected by the secondary component seen in NOEMA H¹³CO⁺ is avoided to produce the median radial profile (see Sect. 3.1.3). ^(‡) [Palmeirim et al. \(2013\)](#). ^(*) $D_{\text{HP}}^{\text{Plummer}}$ value obtained by fitting the northeastern and southwestern sides of the median radial profile simultaneously. Due to differing p indices, this is not a simple average of the $D_{\text{HP}}^{\text{Plummer}}$ values given in Cols. [2] and [3].

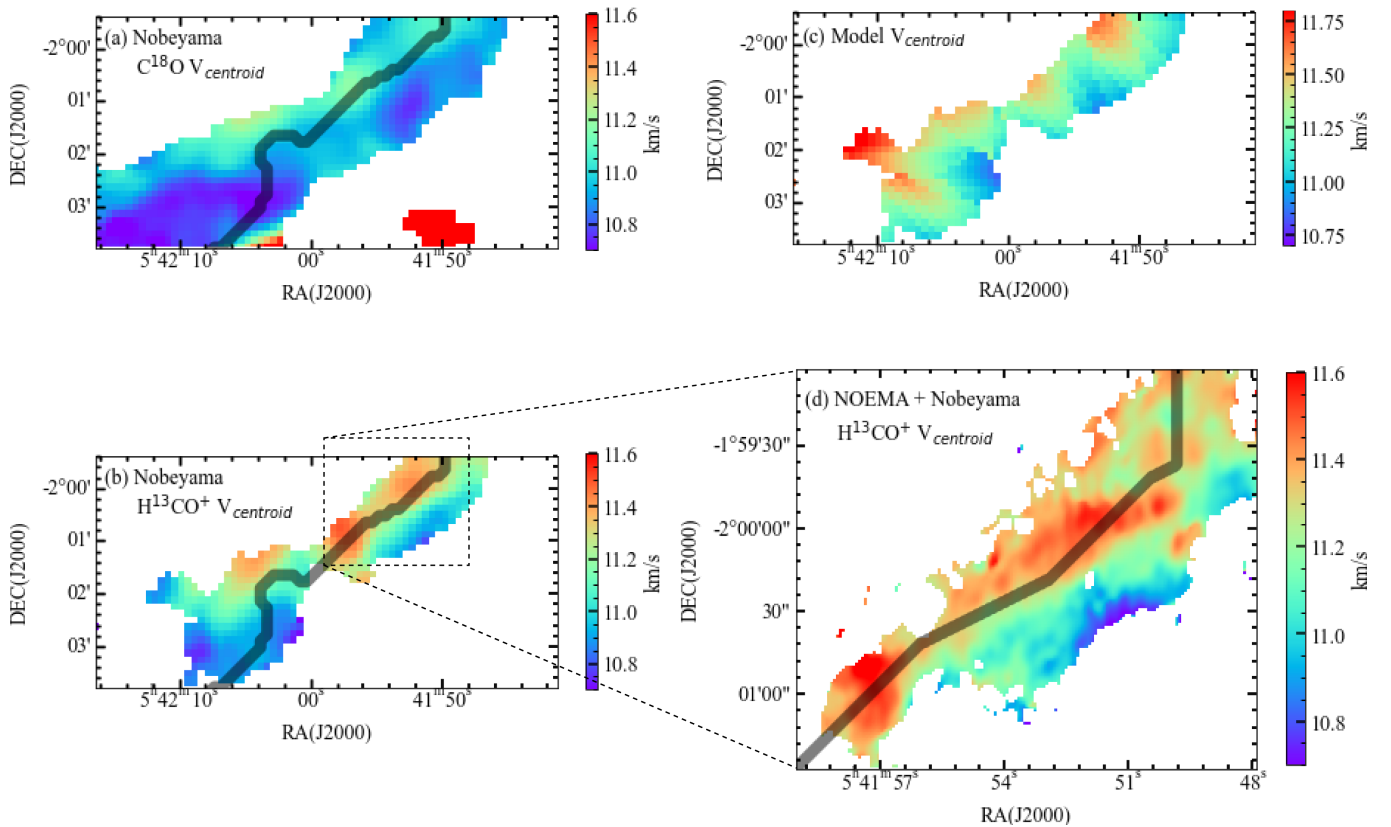


Fig. 7. (a) Nobeyama C¹⁸O (1–0) centroid velocity map, (b) Nobeyama H¹³CO⁺ (1–0) centroid velocity map (close-up view of panel b in Fig. 4), (c) centroid velocity map of the fragmenting filament model, and (d) NOEMA+45m H¹³CO⁺ (1–0) centroid velocity map toward the NOEMA observed area indicated by the dashed box in panel b. In panels a and b, a black line indicates the crest of the filament which corresponds to the z -axis in Fig. 8a and $r = 0$ in Fig. 8b. The back line starts at $(\text{RA}_{\text{J2000}}, \text{Dec}_{\text{J2000}}) = (5^{\text{h}}42^{\text{m}}11^{\text{s}}.823, -2^{\circ}02^{\text{m}}53^{\text{s}}.97)$ and ends at $(\text{RA}_{\text{J2000}}, \text{Dec}_{\text{J2000}}) = (5^{\text{h}}41^{\text{m}}45^{\text{s}}.806, -1^{\circ}59^{\text{m}}23^{\text{s}}.97)$. See also Fig. A.1.

Figure 8a shows the variations in Nobeyama H¹³CO⁺ and C¹⁸O centroid velocities along the NGC 2024S filament (z -axis). A velocity oscillation pattern can be recognized along the filament. Using the following fitting function⁷ (see [Peretto et al. 2015](#)):

$$V(z) = V_{\text{sys}} + z \nabla V_z + V_0 \cos(2\pi z / \lambda + \theta_{\text{offset}}), \quad (6)$$

the best-fit velocity gradient along the filament ∇V_z was found to be 0.29 ± 0.17 km s⁻¹ pc⁻¹ in H¹³CO⁺ and 0.51 ± 0.06 km s⁻¹

⁷ For the fitting, we used the python `scipy.optimize.curve_fit` package.

pc⁻¹ in C¹⁸O. The amplitude (V_0) of the oscillation was found to be 0.15 ± 0.08 km s⁻¹ in H¹³CO⁺ and 0.10 ± 0.02 km s⁻¹ in C¹⁸O, respectively. The wavelength (λ) of the oscillation pattern was found to be 0.21 ± 0.01 pc in H¹³CO⁺ and 0.26 ± 0.01 pc in C¹⁸O, respectively. The positions of the dense cores identified by [Könyves et al. \(2020\)](#) the HGBS data are indicated by vertical gray strips at $z = 0.48$ pc (HGBS 054203.2-02035), $z = 0.81$ pc (HGBS054157.3-020101), $z = 0.96$ pc (HGBS 054153.4-020016), and $z = 1.10$ pc (HGBS 054149.5-015941). They are slightly shifted from the observed centroid velocity peaks in H¹³CO⁺ or C¹⁸O. Table 6 summarizes the offsets between the *Herschel*

Table 6. Positional offsets between column density and velocity peaks.

λ		HGBS 054203.2-02035	HGBS 054157.3-020101	HGBS 054153.4-020016	HGBS 054149.5-015941
<i>Herschel</i> column density	–	peak $z=0.48$ pc	peak $z=0.81$ pc	peak $z=0.96$ pc	peak $z=1.10$ pc
Nobeyama H ¹³ CO ⁺	0.21 pc	peak(obs./fit) offset(obs./fit) in pc offset(obs./fit) in λ offset(obs./fit) in λ ^(†)	peak(obs./fit) offset(obs./fit) in pc offset(obs./fit) in λ offset(obs./fit) in λ ^(†)	peak(obs./fit) offset(obs./fit) in pc offset(obs./fit) in λ offset(obs./fit) in λ ^(†)	peak(obs./fit) offset(obs./fit) in pc offset(obs./fit) in λ offset(obs./fit) in λ ^(†)
Nobeyama C ¹⁸ O	0.26 pc	peak(obs./fit) offset(obs./fit) in pc offset(obs./fit) in λ offset(obs./fit) in λ ^(†)	peak(obs./fit) offset(obs./fit) in pc offset(obs./fit) in λ offset(obs./fit) in λ ^(†)	peak(obs./fit) offset(obs./fit) in pc offset(obs./fit) in λ offset(obs./fit) in λ ^(†)	peak(obs./fit) offset(obs./fit) in pc offset(obs./fit) in λ offset(obs./fit) in λ ^(†)

Notes. z measures position along the filament crest shown in Fig. 1. The uncertainties of the positional offsets in units of λ were estimated assuming that the peaks in column density have an uncertainty corresponding to half a beam. ^(†): Given the additional errors arising from the definition of the curved filament crest around HGBS 054203.2-02035, we also provide offsets estimated assuming a straight filament crest toward this core (see text in Sect. 4.2.1).

column density peaks and the Nobeyama 45m H¹³CO⁺ and C¹⁸O peaks. Here, z measures position along the filament crest shown in Fig. 1 and $z = 0$ pc corresponds to southeastern edge of the filament crest. The positional offset between the peak in column density and that in centroid velocity for HGBS 054203.2-02035 is about -0.1 pc, roughly corresponding to $-0.5 \pm 0.1 \lambda$ in H¹³CO⁺ and about -0.13 pc, roughly corresponding to $-0.5 \pm 0.1 \lambda$ in C¹⁸O. The positional offset for HGBS 054157.3-020101 is -0.020 pc in the observed velocity pattern and -0.04 pc in the fitted velocity pattern, roughly corresponding to $\sim -0.1-0.2\lambda$, in C¹⁸O, while the *Herschel* dense core located at 0.81 pc coincides with the peak in H¹³CO⁺ centroid velocity. The positional difference for HGBS 054153.4-020016 is -0.062 pc, roughly corresponding to $-1/4 \lambda$, in H¹³CO⁺, while the C¹⁸O emission does not show a clear peak in centroid velocity. The positional difference for HGBS 054149.5-015941 is -0.03 pc in the observed velocity pattern, roughly corresponding to -0.1λ and -0.04 pc in the observed velocity pattern corresponding to $\sim -0.2\lambda$ in C¹⁸O, while the H¹³CO⁺ emission does not show clear peak in centroid velocity. This source is associated with a *Spitzer* protostar in the catalog of Megeath et al. (2012).

Figure 8b shows the variations in NOEMA+45m H¹³CO⁺ centroid velocity along the NGC 2024S filament (z -axis). The distribution of the NOEMA+45m H¹³CO⁺ centroid velocity is consistent with that of the Nobeyama H¹³CO⁺ centroid velocity. Only three cores are covered because of the limited extent of the NOEMA observations. However, the velocity pattern seen in the NOEMA+45m H¹³CO⁺ data is more nicely fitted than the Nobeyama H¹³CO⁺ pattern.

Figure 8c shows the variations in H¹³CO⁺ centroid velocity along the minor axis of the filament (r direction), confirming the presence of a transverse velocity gradient (i.e., the centroid velocity is redshifted to the northeast of the filament crest, while it is blueshifted to the southwest of the crest). We note that this velocity gradient has a direction opposite to that seen on larger (parsec) scales as described in Sect. 3.1.1 (see Fig. 3). Indeed, the maps observed in CO (and isotopes) show emission at redshifted velocities to the southwest of the filament (Figs. 2d, i, n) and blueshifted velocities to the northeast of the filament (Figs. 2b, g, l). In addition, the dimensionless coefficient $C_v \equiv \frac{\delta V^2}{GM_{\text{line}}}$ introduced by Chen et al. (2020), where δV is half of the velocity difference across the filament, is estimated to be much less than 1 ($C_v = 0.12$), suggesting that the transverse velocity gradient observed in H¹³CO⁺ on small scales is driven by self-gravity as opposed to large-scale shock compression. The H¹³CO⁺ velocity

gradient may reflect the bulk motion of the filament itself (e.g., possibly the rotation of the filament about its main axis; (cf., Matsumoto et al. 1994; Dhabal et al. 2018; Hsieh et al. 2021), although this would require confirmation.

For simplicity, we fitted the centroid velocities observed along the minor axis of the filament assuming a constant transverse velocity gradient ∇V_r , as in the following equation:

$$V(r) = V_{\text{sys}} + r \nabla V_r. \quad (7)$$

The best-fit transverse velocity gradient (in the r direction) is found to be $2.72 \pm 0.15 \text{ km s}^{-1} \text{ pc}^{-1}$. It is worth noting that this transverse velocity gradient is an order of magnitude higher than the longitudinal velocity gradient of $0.29 \pm 0.17 \text{ km s}^{-1} \text{ pc}^{-1}$. The fit parameters are summarized in Table 7. For comparison, the transverse velocity gradients observed in the Orion A integral-shaped filament and in the SDC13 infrared dark filament are measured to be $\sim 1.0 \text{ km s}^{-1}$ in H¹³CO⁺ (1–0) and $0.2-1.5 \text{ km s}^{-1} \text{ pc}^{-1}$ in NH₃ (1,1), (Ikeda et al. 2007; Williams et al. 2018), respectively.

Figure 8 also shows the variations in C¹⁸O centroid velocity along (panel a) and across (panel c) the filament. In both directions, the C¹⁸O centroid velocities differ somewhat the centroid velocities observed in H¹³CO⁺. Possible reasons why the C¹⁸O and H¹³CO⁺ centroid velocities exhibit slightly different patterns are that (i) the C¹⁸O molecule may be depleted in the inner part of the filament as described in Sect. 3.1.2, and (ii) the C¹⁸O emission preferentially traces the outer parts of the filament compared to the H¹³CO⁺ emission as described in Sect. 3.1.5.

We also derived a velocity structure function (VSF), $S_2(l)$, from the Nobeyama H¹³CO⁺ data. The function $S_2(l)$ at each scale l can be defined as follows (cf. Peretto et al. 2015; Henshaw et al. 2020):

$$S_2(l) = \text{median} \left([V(x_i, y_i + l) - V(x_i, y_i)]^2 \right), \quad (8)$$

where (x_i, y_i) are the coordinates of each position and l denotes the separation between positions.

Figure 9 shows the observed VSF of the Nobeyama H¹³CO⁺ velocity components. The VSF increases up to 0.2 km s^{-1} for $l < \sim 0.15$ pc, then increases more gradually with small oscillations for $\sim 0.15 \text{ pc} \leq l < \sim 0.6$ pc, and finally increases steadily again for $\sim 0.6 \text{ pc} \leq l$.

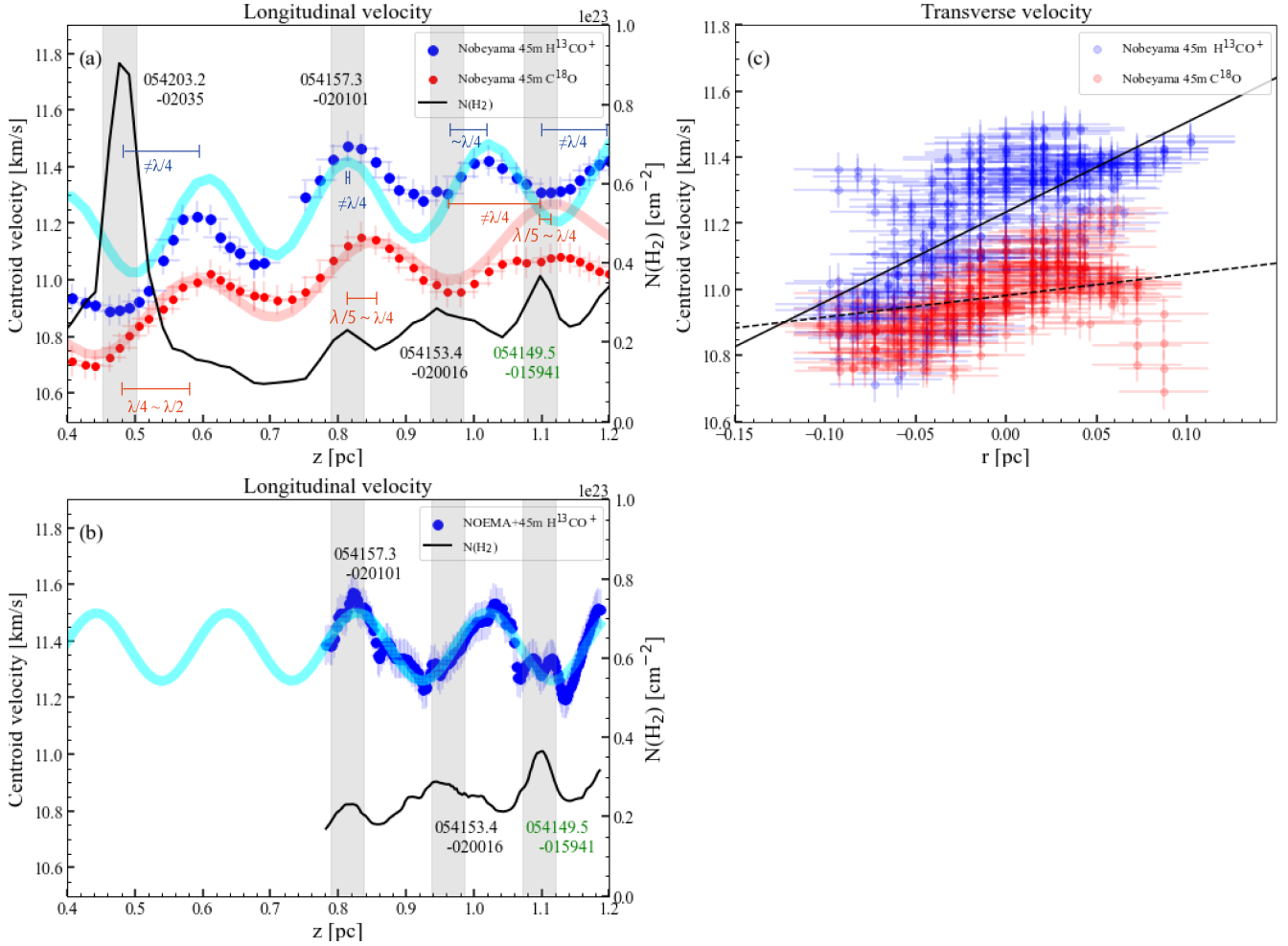


Fig. 8. (a) Nobeyama 45m H^{13}CO^+ (1–0) and C^{18}O (1–0) centroid velocities along the filament, (b) NOEMA+45m H^{13}CO^+ (1–0) centroid velocities along the filament, and (c) Nobeyama 45m H^{13}CO^+ (1–0) and C^{18}O (1–0) centroid velocities along the r direction. In each panel, blue and red points indicate the centroid velocity of H^{13}CO^+ and C^{18}O , respectively. In panels a and b, the blue and red curves show the result of the least square fitting with a function of $v(z) = V_{\text{sys}} + z\nabla V_z + V_0 \cos(2\pi z/\lambda + \theta_{\text{offset}})$ against the H^{13}CO^+ (1–0) and C^{18}O (1–0) centroid velocity. In panels a and b, the black curves indicate the distribution of *Herschel* H_2 column density along the filament in the $25''$ resolution map. The vertical gray strips indicate the positions of *Herschel* dense cores identified by Könyves et al. (2020, HGBS 054203.2–020235, 054157.3–020101, 054153.4–020016, and 054149.5–015941). The width of each strip corresponds to a $25''$ beam. The core labeled in green is associated with a *Spitzer* protostar (Megeath et al. 2012). In this plot, z measures the position along the magenta curve in Fig. 1, and $z=0$ corresponds to the southeastern edge of the curve. Each data point is on the crest of the filament. In panel c, the two solid and dashed lines show the best-fit transverse velocity gradient of the form $V(r) = V_{\text{sys}} + r\nabla V_r$ observed in H^{13}CO^+ (1–0) and C^{18}O (1–0), respectively. $r=0$ corresponds to the crest of the filament as indicated by the magenta curve in Fig. 1. All pixels in the maps of Figs. 7a, b, and d are used for this plot by estimating the projected separation from the filament crest.

4. Discussion

4.1. Variations in filament width among tracers

As described in Sect. 3, filamentary structures are detected in the Nobeyama ^{13}CO (1–0), C^{18}O (1–0), and H^{13}CO^+ (1–0) data. Panopoulou et al. (2014) measured the widths of ^{13}CO (1–0) filamentary structures in the Taurus molecular cloud and found a typical value of 0.4 pc, while Palmeirim et al. (2013) found a filament width of ~ 0.1 pc from the *Herschel* column density map of the Taurus B211/213 region. Using N_2H^+ (1–0) and H^{13}CO^+ (1–0) intensity maps of the Serpens Main, Perseus, and Orion A molecular clouds, Lee et al. (2014), Dhabal et al. (2018), and Hacar et al. (2018) reported a typical filament width of ~ 0.035 pc, which is narrower than the value of ~ 0.1 pc found for *Herschel* filaments (Arzoumanian et al. 2011, 2019). In order to investigate whether these differences in filament width estimates

arise from using different tracers, we fitted the integrated intensity profiles observed in ^{13}CO (1–0), C^{18}O (1–0), and H^{13}CO^+ (1–0) on the northeastern side of the NGC 2024S filament in the same manner as in Sect. 3.1.5 for the column density profiles:

$$W_{\text{mol}}(r) = \frac{W_{\text{mol}}^0}{\left[1 + (r/R_{\text{flat}})^2\right]^{\frac{p-1}{2}}}, \quad (9)$$

where $W_{\text{mol}}(r)$ is the integrated intensity of each observed molecular transition. To compare the widths of the filament obtained from the ^{13}CO (1–0), C^{18}O (1–0), *Herschel* column density, and H^{13}CO^+ (1–0) maps, we fitted the data at the same angular resolution of $25''$. We found $D_{\text{HP}}^{\text{Plummer}}$ values of 0.694 ± 0.485 pc in ^{13}CO , 0.251 ± 0.021 pc in C^{18}O , 0.097 ± 0.012 pc with *Herschel*, and 0.063 ± 0.012 pc in H^{13}CO^+ , respectively (see also Fig. 10

Table 7. Fitting results for the distribution of observed centroid velocities.

Line	H ¹³ CO ⁺ (1–0)	C ¹⁸ O(1–0)
$(V(r) = V_{\text{sys}} + r\nabla V_r)$		
Transverse velocity gradient		
V_{sys}	11.23±0.01 km s ⁻¹	10.98±0.01 km s ⁻¹
∇V_r	2.72±0.15 km s ⁻¹ pc ⁻¹	0.65±0.19 km s ⁻¹ pc ⁻¹
$(V(z) = V_{\text{sys}} + z\nabla V_z + V_0 \cos(2\pi z/\lambda + \theta_{\text{shift}}))$		
Longitudinal velocity gradient		
V_{sys}	11.03±0.14 km s ⁻¹	10.64±0.05 km s ⁻¹
∇V_z	0.29±0.17 km s ⁻¹ pc ⁻¹	0.51±0.06 km s ⁻¹ pc ⁻¹
V_0	0.15±0.08 km s ⁻¹	0.10±0.02 km s ⁻¹
λ	0.21±0.01 pc	0.26±0.01 pc
θ_{offset}	0.55±1.46 rad	4.90±0.64 rad

Notes. The fitting was performed on independent centroid velocity measurements (i.e., separated by more than a beam size). Quoted errors are formal statistical errors corresponding to the square roots of the diagonal elements in the covariance matrix of fitted parameters returned by the *scipy curve_fit* routine. Total errors may be larger.

Table 8. Comparison of width estimates among tracers for the NGC 2024S filament.

Tracer	Beam size (")	Beam size (pc)	$D_{\text{HP}}^{\text{Plummer}}$ (pc) (*)	p
ArTéMiS+ <i>Herschel</i>	8"	~0.015	0.081±0.014	1.9±0.2
<i>Herschel</i>	18".2	~0.035	0.080±0.010	1.7±0.1
<i>Herschel</i>	25".0	~0.048	0.097±0.012	1.7±0.1
H ¹³ CO ⁺ (1–0) ^(†)	6".40×3".7	~0.011 × 0.007	0.047±0.005	2.5±0.2
H ¹³ CO ⁺ (1–0)	25".0	~0.048	0.063±0.012	2.5±0.4
C ¹⁸ O(1–0)	25".0	~0.048	0.251±0.021	2.5±0.2
¹³ CO(1–0)	25".0	~0.048	0.694±0.485	2.5±1.0

Notes. (*) Deconvolved from the beam size. (†) NOEMA+45m H¹³CO⁺(1–0) integrated intensity map.

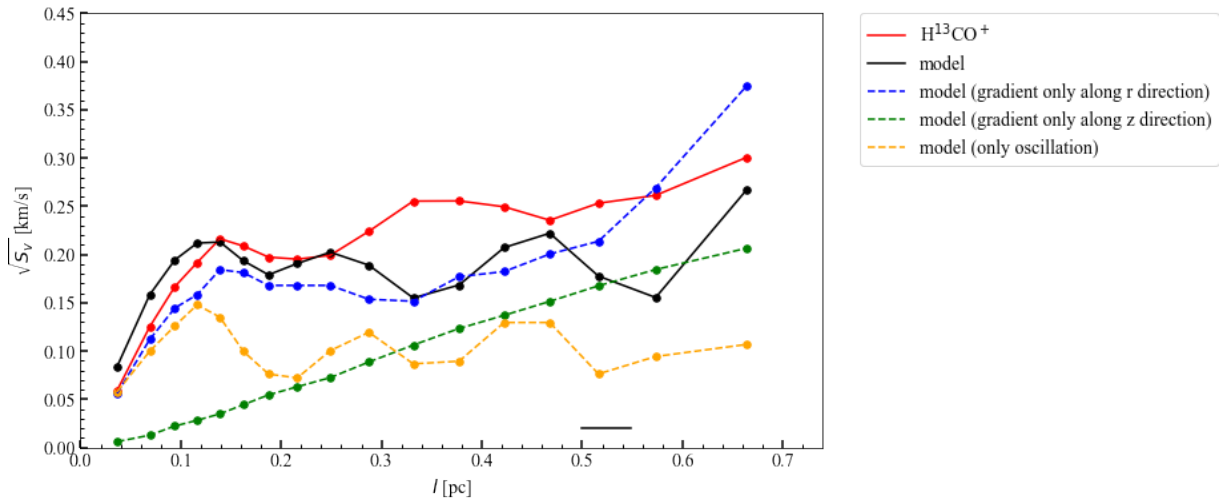


Fig. 9. Comparison of the VSF between Nobeyama H¹³CO⁺ (1–0) data and the model. The red line and points indicate the VSF of the Nobeyama H¹³CO⁺ (1–0) centroid velocity. The black line and points indicate the VSF of the modeled fragmenting filament. Blue, green, and dashed blue lines indicate the VSF of the models in which only the velocity gradient along the r direction, the velocity gradient along the z direction, and the oscillation are taken into account, respectively. The typical uncertainty of the observed VSF is 0.08 km s⁻¹.

and Table 8). The measured $D_{\text{HP}}^{\text{Plummer}}$ width is only marginally resolved in the Nobeyama H¹³CO⁺ (1–0) data at 25" resolution (~0.048 pc). Therefore, we also fitted the NOEMA+45m H¹³CO⁺ data at an angular resolution of ~6".4×3".7 (0.012 pc × 0.006 pc). We found a $D_{\text{HP}}^{\text{Plummer}}$ value of 0.047±0.005 pc, which is a factor of 2 lower than the $D_{\text{HP}}^{\text{Plummer}}$ width measured

in the *Herschel* column density map. The ¹³CO (1–0), C¹⁸O (1–0), and H¹³CO⁺ (1–0) data trace emission regions of density ~10³ cm⁻³, ~10³⁻⁴ cm⁻³, ~10³⁻⁵ cm⁻³, respectively (Onishi et al. 1998; Yonekura et al. 2005; Ikeda et al. 2007; Maruta et al. 2010; Qian et al. 2012; Shimajiri et al. 2015). Our results for the NGC 2024S filament (see, e.g., Fig. 10) confirm that

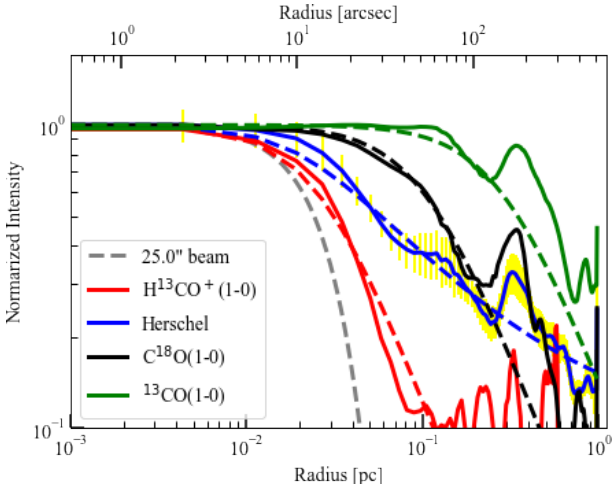


Fig. 10. Comparison of median radial column density profiles for the northeastern side of the NGC 2024S filament among *Herschel* column density (blue), H^{13}CO^+ (red), C^{18}O (black), and ^{13}CO (green) at a resolution of $25''$ (~ 0.048 pc). The dashed curves show the best-fit Plummer model. The yellow bars show the dispersion ($\pm 1\sigma$) of the distribution of the radial profile along the filament in *Herschel*. The gray curves indicate the angular resolution of $25''$. Note that we reproduced the Nobeyama H^{13}CO^+ map with an angular resolution of $25''$ to compare it with others in the same angular resolution.

filament widths measured in dense gas tracers such as N_2H^+ (1–0) and H^{13}CO^+ (1–0) tend to be narrower than those found using tracers of low-density gas such as ^{13}CO (1–0) and C^{18}O (1–0), (Panopoulou et al. 2014; Lee et al. 2014; Dhabal et al. 2018; Hacar et al. 2018). The observed differences in filament width measurements among tracers are likely due to differences in the range of densities probed by each tracer. The Nobeyama ^{13}CO (1–0) and C^{18}O (1–0) data trace the outer (lower density) part of the *Herschel* filament and the Nobeyama/NOEMA H^{13}CO^+ (1–0) emission trace the inner (denser) part. This also shows that it is important to compare measurements obtained with the same tracer when discussing the universality (or non-universality) of filament widths. The filament profiles obtained in any given molecular line tracer are affected by a limited dynamic range in density, as described above, and are sensitive to chemical effects such as depletion (Bergin et al. 2002; Tafalla et al. 2002) or far-ultraviolet photo-dissociation (Lada et al. 1994; Shimajiri et al. 2014; Lin et al. 2016). Using $\text{N}(\text{H}_2)$ column density profiles derived from high dynamic range submillimeter dust continuum maps (from, e.g., *Herschel*) provides more reliable estimates of filament widths.

The $D_{\text{HP}}^{\text{Plummer}}$ width we measure here in C^{18}O (1–0) for the NGC 2024S filament is 0.2 pc, while a more “typical” filament width of $\sim 0.12 \pm 0.04$ pc (FWHM) was reported by Orkisz et al. (2019) based on Gaussian fitting for a sample of C^{18}O (1–0) filaments observed with the IRAM 30m telescope in Orion B. In the Orkisz et al. study, the FWHM widths of filaments in the NGC 2024 subregion tend to be broader than the “typical” value in the sample and reach up to 0.2 pc. Thus, our C^{18}O (1–0) findings for NGC 2024S are consistent with the results of Orkisz et al. (2019).

It is also worth comparing the half-power diameter of the NGC 2024S filament in Orion B with the filament widths found in the Orion A molecular cloud. Recently, Schuller et al. (2021) measured the distribution of filament half-power diameters in the northern part of the integral-shaped filament of the Orion A

molecular cloud using APEX/ArTéMiS 350 and $450 \mu\text{m}$ data combined with *Herschel*/SPIRE data, providing an angular resolution of $8''$ (corresponding to 0.015 pc at a distance of 410 pc, Menten et al. 2007). They found that half-power diameters ranging from 0.06 pc to 0.11 pc and line masses in the range ~ 100 – $500 M_{\odot} \text{pc}^{-1}$. The half-power diameters of the massive star-forming filament in NGC 6334 ($M_{\text{line}} = 600$ – $1200 M_{\odot} \text{pc}^{-1}$ rescaled to a distance of 1.35 kpc; Chibueze et al. 2014) and the low-mass star-forming filament B211/B213 in Taurus ($M_{\text{line}} = 54 M_{\odot} \text{pc}^{-1}$) have been measured to be $D_{\text{HP}}^{\text{Plummer}} = 0.12 \pm 0.03$ pc (at $d = 1.35$ kpc) and $D_{\text{HP}}^{\text{Plummer}} = 0.11 \pm 0.02$ pc, respectively. The half-power diameter of 0.081 ± 0.014 pc reported here for the NGC 2024S filament ($M_{\text{line}} = 62 M_{\odot} \text{pc}^{-1}$) is consistent with the values found in the integral-shaped filament. We conclude that the half-power diameters measured from submillimeter dust continuum data are consistent among filaments spanning a wide range of line masses.

4.2. Filament fragmentation

As described in Sect. 3.2, a positional offset is seen between the peak in H^{13}CO^+ (1–0) integrated intensity and the peak in H^{13}CO^+ (1–0) centroid velocity. Furthermore, the centroid velocity observed along the NGC 2024S filament exhibits an oscillation pattern. A similar velocity structure was reported by Hacar & Tafalla (2011) for a filament in the Taurus/L 1517 region. In L 1517, a $\lambda/4$ phase shift was observed between the density and the velocity field around the cores forming along the filament axis. Hacar & Tafalla (2011) argued that the L 1517 filament was in the process of fragmenting owing to gravitational instability. Here, we similarly discuss whether the NGC 2024S filament may be fragmenting into cores due to gravitational instability based on a comparison between the density and the velocity field (Sect. 4.2.1), and a comparison of the observed VSF with that of a toy model of a fragmenting filament (Sect. 4.2.2).

4.2.1. Fragmentation by gravitational instability?

As discussed in Sect. 3.2 (see, e.g., Fig. 8a), a positional offset is observed between the column density peaks and the peaks in either the H^{13}CO^+ or C^{18}O centroid velocity, or both. A $\lambda/4$ phase shift between the density and the velocity field is expected for core-forming motions in a filament fragmenting into condensations (cf. Gehman et al. 1996; Hacar & Tafalla 2011). For cores to be forming, gas motions have to converge into the core centers. Therefore, the density peak associated with a forming core has to correspond to a position of vanishing velocity. This requires a $\lambda/4$ phase shift between the density and the centroid velocity under the assumption that the density and velocity perturbations are sinusoidal. The condensation seen in the *Herschel* column density map at $z = 0.96$ pc (HGBS 054153.4-020016) shows a $\lambda/4$ phase shift between the density and the H^{13}CO^+ centroid velocity and corresponds to a protostar identified by Megeath et al. (2012). This supports the view that the observed velocity and column density patterns trace the convergence of matter onto the corresponding protostellar core. However, a clear C^{18}O velocity peak associated with HGBS 054153.4-020016 is not observed. In the case of the HGBS 054157.3-020101 condensation, the column density peak coincides with the H^{13}CO^+ velocity peak, while a $\sim \lambda/5$ - $\lambda/4$ phase shift is observed between the column density and C^{18}O velocity peaks. For HGBS 054149.5-015941, a $\sim \lambda/5$ - $\lambda/4$ phase shift between the column density and C^{18}O velocity peaks is also observed but is not seen in H^{13}CO^+ . For HGBS 054203.2-02035, the phase shift is almost $\lambda/2$ in

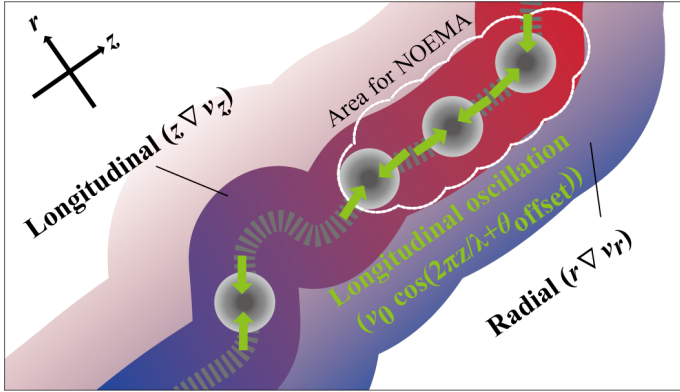


Fig. 11. Schematic picture of the velocity structure in NGC 2024S based on our observational results. Darker red and blue colors indicate the velocity gradient in the longitudinal direction. Lighter red and blue colors indicate the velocity gradient in the radial direction. A dashed gray line marks the crest of the filament. Filled gray circles indicate the cores. Green arrows indicate the velocity oscillation along the filament. A white polygon indicates the area observed with NOEMA.

both H^{13}CO^+ and C^{18}O . However, the precise location of the filament crest around HGBS 054203.2-02035 is uncertain due to, for example, the lower column density of the filament between HGBS 054203.2-02035 and HGBS 054157.3-020101. While the nominal crest orientation around HGBS 054203.2-02035 is almost south to north, the overall crest orientation of the NGC 2024S filament is from southeast to northwest. The actual filament crest around HGBS 054203.2-02035 is believed to be located somewhere in between the south-north and southeast-northwest directions. Assuming a straight crest from southeast to northwest, the column density and velocity peaks almost coincide in both H^{13}CO^+ and C^{18}O (i.e., $\sim 0.25\lambda$ shift). Therefore, given the uncertainty in the exact location of the filament crest, an actual shift $\sim \lambda/4$ cannot be ruled out for HGBS 054203.2-02035. To summarize, a $\sim \lambda/4$ shift is observed around HGBS 054153.4-020016 in H^{13}CO^+ and the data around HGBS 054203.2-02035, 054157.3-02010, and 054149.5-015941 are marginally consistent with $\sim \lambda/4$ shifts in C^{18}O given the error bars, but there is no evidence of a $\sim \lambda/4$ shift in H^{13}CO^+ around HGBS 054203.2-02035, 054157.3-02010, 054149.5-015941, nor in C^{18}O around HGBS 054153.4-020016. The difference between H^{13}CO^+ and C^{18}O patterns may arise from differences in the range of densities probed by H^{13}CO^+ and C^{18}O as discussed in Sect. 4.1.

In the quasi-static fragmentation model of Gehman et al. (1996), a systematic phase shift of $\lambda/4$ between the density and velocity peaks is expected for all cores. Here, a $\lambda/4$ shift is not observed for all cores in any single tracer although it is tentatively observed for all cores in either H^{13}CO^+ or C^{18}O . Thus, the physical structure of the NGC 2024S filament is clearly more complex than the prediction of the simple quasi-static fragmentation model. Strictly speaking, the quasi-static model discussed by Gehman et al. (1996) is only expected to apply to isolated, nearly isothermal filaments close to hydrostatic equilibrium. In the case of the NGC 2024S filament, both the line mass ($M_{\text{line}} \sim 62 M_{\odot} \text{pc}^{-1}$) and the index of the radial density profile ($p \sim 2$) differ from the thermally critical line mass $M_{\text{line,crit}} \equiv 2c_s^2/G \sim 16 M_{\odot} \text{pc}^{-1}$ and $p = 4$ value expected for an isothermal filament in hydrostatic equilibrium (cf. Ostriker 1964). The NGC 2024S filament is nevertheless close to virial equilibrium with $M_{\text{line}} \sim M_{\text{line,vir}} \equiv 2\sigma^2/G$ (Fiege & Pudritz 2000, see also Sect. 3.1.5). Moreover, both polytropic and

magnetized equilibrium filaments may have $p \sim 2$ as observed for NGC 2024S (cf. Kawachi & Hanawa 1998; Palmeirim et al. 2013; Kashiwagi & Tomisaka 2021). A more important difference perhaps with the idealized quasi-static model of Gehman et al. (1996) is that the NGC 2024S filament is not isolated but embedded in the turbulent environment of the Orion B cloud and may be accreting from this environment. As illustrated by the numerical simulations of Clarke et al. (2016) and Anathpindika & Di Francesco (2021), the ambient environment may modify the fragmentation properties of a filament.

4.2.2. Modeling the fragmenting filament

To examine whether the observed velocity pattern can be explained by filament fragmentation, we modeled the velocity field in and around the filament taking four velocity components into account (cf. Peretto et al. 2015):

$$V(z, r) = V_{\text{sys}} + r\nabla V_r + z\nabla V_z + V_0 \cos(2\pi z/\lambda + \theta_{\text{offset}}). \quad (10)$$

The first term on the right hand side of Eq. (10) expresses the systemic velocity of the cloud. The second and third terms express transverse and longitudinal velocity gradients, respectively. The fourth term expresses a longitudinal oscillation caused by fragmentation of the filament into cores. z and r denote the longitudinal (major axis of the filament) and the radial (minor axis of the filament) direction, respectively. ∇V_r and ∇V_z are the velocity gradients along the radial and longitudinal directions, respectively. V_0 and λ are the amplitude and wavelength of the longitudinal oscillations. The values of ∇V_z , ∇V_r , V_0 , and λ were obtained from the fitting results (see Sect. 3.2, Table 7, and Fig. 8). Figure 11 shows a schematic picture of the velocity structure in NGC 2024S based on our observational results. Figures 7c and 7d show the centroid velocity map of the toy model and that of the Nobeyama H^{13}CO^+ (1–0) data, respectively. It can be seen that the observed distribution of H^{13}CO^+ centroid velocities is similar to that of the model.

To get further insight into the physical meaning of the observed velocity structure (see Sect. 3.2), we compared the observed VSF to the VSF obtained from our toy model, as well as single-component models taking each velocity component separately into account.

Figure 9 compares the observed VSF from the Nobeyama H^{13}CO^+ data cube with the VSF of the model including the above three velocity components [black curve – see Eq. (10)]. The VSF of the model, $[S_2(l)]^{1/2}$, increases up to 0.2 km s^{-1} for $l < \sim 0.15 \text{ pc}$, then increases more gradually with small oscillations for $\sim 0.15 \text{ pc} \leq l < \sim 0.6 \text{ pc}$, and finally increases steadily again for $\sim 0.6 \text{ pc} \leq l$. We also show in Fig. 9 the VSFs of each model component separately: (i) the transverse velocity component (blue curve), (ii) the longitudinal velocity component (green curve), and (iii) the longitudinal oscillation component caused by fragmentation (yellow curve). Among the single-component model VSFs, the only VSF showing an oscillation pattern is that of the model with a longitudinal oscillation. The observed H^{13}CO^+ VSF does show an oscillation pattern and is qualitatively very similar to the VSF of our model including all three velocity components (see Fig. 9). This suggests that the oscillation pattern seen in the observed VSF results from the effect of gravitational fragmentation of the NGC2024S filament into cores. Hacar et al. (2016) performed a similar VSF analysis using H^{13}CO (2–1) data toward the 6-pc long filament in the Musca cloud and found that the observed VSF could be described by the superposition of a global velocity gradient along the filament and local velocity oscillations.

4.2.3. Core separation along the filament

When its mass per unit length is close to that required for hydrostatic equilibrium, a filament is expected to fragment into cores with a characteristic spacing of about four times the filament width according to the self-similar models that describe the evolution of isothermal filaments under the influence of self-gravity without magnetic fields or turbulence (Inutsuka & Miyama 1992). As described in Sect. 3.1.5, the filament diameter $D_{\text{HP}}^{\text{Plummer}}$ of NGC 2024S is estimated to be $\sim 0.081 \pm 0.014$ pc. Thus, the typical separation between cores is expected to be ~ 0.32 pc, corresponding to 4 times the observed filament width. Five cores (HGBS 054157.3-020101, 054153.4-020016, 054150.5-020024, 054149.5-015941, and 054203.2-020235) are embedded along the NGC 2024S filament. HGBS 054203.2-020235 is not covered by the NOEMA observations and HGBS 054150.5-020024 may be associated with the secondary component seen in NOEMA H^{13}CO^+ as mentioned in Sect. 3.1.3. The mean separation among the four *Herschel* cores, excluding HGBS 054150.5-020024, is 0.12 ± 0.05 pc. The mean separation among the five *Herschel* cores is 0.13 ± 0.06 pc. These are projected separations that do not take the viewing angle of the filament into account. Assuming the inclination of the filament to the line of sight is $\alpha_0 = 18 \pm 5$ deg, the observed separations would translate into intrinsic separations consistent with ~ 4 times the filament width. However, this would require the NGC 2024S filament to be seen closer to a ‘‘pole-on’’ configuration than to a ‘‘plane-of-sky’’ configuration. Assuming random orientations, the probability of observing a filament with a viewing angle $\alpha \leq \alpha_0$ is $p = 1 - \cos \alpha_0 \sim 5\%$ for $\alpha_0 = 18$ deg. Alternatively, adopting a more likely inclination to the line of sight [e.g., $\alpha_0 \geq 60$ deg, for which $p(\alpha \leq \alpha_0) \geq 50\%$], the observed separations would be indicative of an intrinsic core spacing $\lesssim 0.16$ pc, significantly shorter than the separation predicted by the standard model of filament fragmentation. A similar trend is observed in several other filaments (e.g., Tafalla & Hacar 2015; Zhang et al. 2020).

To test whether the observed separation among cores may be present in the case of randomly distributed cores, we conducted a total of 10 000 realizations of random distributions of 5 sources in a 0.85-parsec-long filament (see Fig. 8a) using the python code FRAGMENT (Clarke et al. 2019) and measured the separation among the randomly placed sources. Comparison between the resulting overall distribution of nearest-neighbor separations and the observed nearest-neighbor-separations distribution using a Kolmogorov-Smirnov test yields a probability or ‘‘ p -value’’ $p = 0.09$ (equivalent to 1.6σ in Gaussian statistics), indicating that the quasi-periodic pattern of the observed cores is only marginally significant. We therefore cannot rule out the possibility that the observed pattern arises from a random distribution.

4.2.4. Relation between core mass and filament line mass

André et al. (2019) proposed that the prestellar core mass function may be inherited from the filament line mass function through gravitational fragmentation of individual filaments and suggested that higher-mass cores may form in higher M_{line} filaments. In their proposed empirical model, the mass of a core formed via fragmentation⁸ of a thermally supercritical but

⁸ In contrast to the idealized model presented by Gehman et al. (1996), recent observations suggest that the gravitational fragmentation of a quasi-equilibrium filament occurs in at least two stages or modes: ‘‘cylindrical’’ fragmentation leads to the formation of clumps along the filament, separated by ~ 4 times the filament width, and subsequent

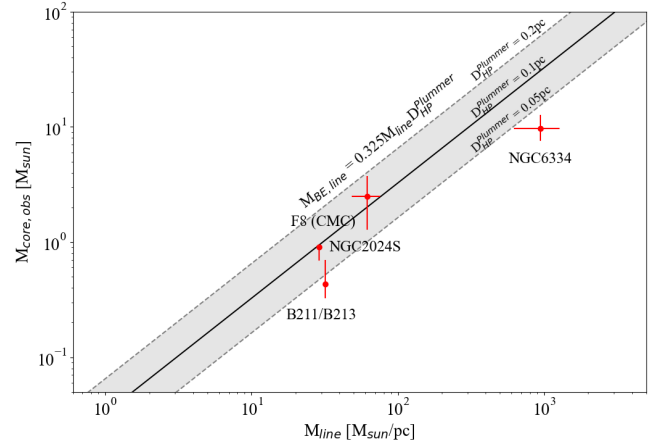


Fig. 12. $M_{\text{core,obs}}-M_{\text{line}}$ relation. The solid black line indicates $M_{\text{BE,eff}} \sim 0.325 M_{\text{line}} D_{\text{HP}}^{\text{Plummer}}$, where $D_{\text{HP}}^{\text{Plummer}} = 0.1$ pc. The dashed black line indicates $M_{\text{BE,eff}} \sim 0.325 M_{\text{line}} D_{\text{HP}}^{\text{Plummer}}$, where $D_{\text{HP}}^{\text{Plummer}} = 0.05$ pc and 0.2 pc. The M_{line} , $M_{\text{core,obs}}$, and their uncertainties for B211/B213, Filament 8 in CMC, and NGC 6334 are from Marsh et al. (2016), Zhang et al. (2020), André et al. (2016), and Shimajiri et al. (2019a).

virialized filament corresponds to the effective Bonnor-Ebert mass $M_{\text{BE,eff}}$ in the filament (see André et al. 2019):

$$M_{\text{BE,eff}} \sim 1.3 \frac{c_{\text{s,eff}}^4}{G^2 \Sigma_{\text{fil}}}, \quad (11)$$

where $c_{\text{s,eff}}$, G , and Σ_{fil} are the one-dimensional velocity dispersion or effective sound speed, the gravitational constant, and the surface density of the filament, respectively. Since the relation $M_{\text{line}} \sim \Sigma_{\text{fil}} \times D_{\text{HP}}^{\text{Plummer}} \sim M_{\text{line,vir}} \equiv 2c_{\text{s,eff}}^2/G$ holds for a thermally supercritical filament (Arzoumanian et al. 2013), we may expect the following relation between the typical core mass and the filament line mass:

$$\left(\frac{M_{\text{BE,eff}}}{[M_{\odot}]} \right) \sim 0.325 \left(\frac{M_{\text{line}}}{[M_{\odot}/\text{pc}]} \right) \times \left(\frac{D_{\text{HP}}^{\text{Plummer}}}{[\text{pc}]} \right). \quad (12)$$

The $D_{\text{HP}}^{\text{Plummer}}$ width of the NGC 2024S filament is measured to be $\sim 0.081 \pm 0.014$ pc. Thus, with $M_{\text{line}} = 62 \pm 13 M_{\odot} \text{ pc}^{-1}$, the core mass in the NGC 2024S filament is expected to be $1.6 \pm 0.4 M_{\odot}$, which agrees very well with the observed mean core mass of $2.5 \pm 1.2 M_{\odot}$.

These findings can be compared to the results of other recent filament fragmentation studies. Our ALMA observations of the NGC 6334 filament (Shimajiri et al. 2019a) revealed 26 compact dense cores with a mean mass of $9.6_{-1.9}^{+3.0} M_{\odot}$ in this massive filament ($M_{\text{line}} = 600\text{--}1200 M_{\odot} \text{ pc}^{-1}$ rescaled to a distance of 1.35 kpc, Chibueze et al. 2014). In their study of the X-shaped nebula in the California molecular cloud, Zhang et al. (2020) identified cores with a mass of $0.9_{-0.2}^{+0.0} M_{\odot}$ within their Filament 8 ($M_{\text{line}} \approx 30 M_{\odot} \text{ pc}^{-1}$). Therefore, we find that there is a suggestive trend of increasing $M_{\text{core,obs}}$ with increasing M_{line} (see Fig. 12), although more data points would be required to be conclusive. The observed $M_{\text{core,obs}}-M_{\text{line}}$ trend is roughly consistent

‘‘spherical’’ fragmentation of the clumps generates Bonnor-Ebert-like cores within clumps (e.g. Kainulainen et al. 2017; Shimajiri et al. 2019a; Clarke et al. 2017). The average core mass is set by the effective critical Bonnor-Ebert mass in the clumps, which is itself related to the local surface density of the filament as per Eq. (11).

with Eq. (12), indicating that higher-mass cores may form in higher M_{line} filaments as proposed by André et al. (2019) and Shimajiri et al. (2019a).

5. Conclusions

To investigate the detailed velocity and density structure of a fragmenting filament in the NGC 2024 region of the Orion B molecular cloud, we performed observations of the ^{12}CO (1–0), ^{13}CO (1–0), C^{18}O (1–0), and H^{13}CO^+ (1–0) molecular lines with the Nobeyama 45m telescope and the NOEMA interferometer. Our main results can be summarized as follows:

- We find that the Nobeyama ^{13}CO (1–0), C^{18}O (1–0), and H^{13}CO^+ (1–0) emission traces the filamentary structure that is seen in the *Herschel* column density map;
- Analysis of the median radial column density profiles of NGC 2024S from ArTéMiS+*Herschel* data yields a half-power diameter of $D_{\text{HP}}^{\text{Plummer}} = \sim 0.081 \pm 0.014$ pc for the filament, which agrees well with the results of previous *Herschel* filament studies in nearby molecular clouds;
- Comparison of the radial profiles derived from *Herschel*, and Nobeyama H^{13}CO^+ (1–0), C^{18}O (1–0), and ^{13}CO (1–0) data shows that measured filament widths can differ depending on the tracer used. Therefore, the same tracer must be employed to discuss the universality (or non-universality) of filament widths. As the filament profiles obtained in any given molecular line tracer are affected by a limited dynamic range in density, using $\text{N}(\text{H}_2)$ column density profiles derived from, for example, *Herschel* dust continuum maps provides more reliable estimates of filament widths;
- Performing a dendrogram analysis, we detected twelve cores in the NOEMA+45m H^{13}CO^+ (1–0) map and four cores in the *Herschel* column density map over the field observed with NOEMA. Each core detected in the *Herschel* column density map corresponds to only one core detected by NOEMA, suggesting that the *Herschel* cores do not have significant substructure;
- The centroid velocity distribution along the major axis of the filament shows an oscillation pattern and a tentative $\lambda/4$ phase shift compared to the density distribution. This $\lambda/4$ shift is not simultaneously observed for all cores in any single tracer but is tentatively seen for each core in either H^{13}CO^+ or C^{18}O . The difference between the H^{13}CO^+ and C^{18}O velocity patterns may arise from differences in the range of densities probed by H^{13}CO^+ and C^{18}O . These results are consistent with the NGC 2024S filament being in the process of fragmenting into cores;
- We modeled the velocity field of the filament and compared the resulting synthetic VSFs with that observed in H^{13}CO^+ . In our toy model, we took the following three velocity components into account: a transverse velocity gradient, a longitudinal velocity gradient, and a longitudinal oscillation caused by fragmentation. The VSF of the Nobeyama H^{13}CO^+ centroid velocity data shows a longitudinal oscillation pattern reminiscent of that produced by fragmentation in the model. This suggests that our observations partly trace core-forming motions resulting from the fragmentation of the NGC 2024S filament into cores. The real physical structure of the NGC2024S filament is nevertheless more complex than the prediction of our simple toy model;
- The average core mass observed in NGC 2024S agrees well with the effective Bonnor-Ebert mass in the filament. Based on a correlation between the typical core mass and the mass per unit length observed for the Taurus B211/B213,

X-shaped California, NGC 2024S, and NGC 6334 filaments, we suggest that higher-mass cores may form in higher- M_{line} filaments, we suggest that higher-mass cores may form in higher- M_{line} filaments.

Acknowledgements. The 45-m radio telescope is operated by Nobeyama Radio Observatory, a branch of National Astronomical Observatory of Japan. The authors are grateful to B. Ladjelate for useful discussions. This work was supported by the ANR-11-BS56-010 project “STARFICH” and the European Research Council under the European Union’s Seventh Framework Programme (ERC Advanced Grant Agreement no. 291294 – ‘ORISTARS’). YS also received support from the ANR (project NIKAS2SKY, grant agreement ANR-15-CE31-0017). This work was supported by NAOJ ALMA Scientific Research Grant Numbers 2017-04A and JSPS KAKENHI Grant Numbers JP19K23463, JP20K04035, and JP21H00057. We also acknowledge support from “Île de France” regional funding (DIM-ACAV+ Program) and from the French national programs of CNRS/INSU on stellar and ISM physics (PNPS and PCMI).

References

- Anathpindika, S. V., & Di Francesco, J. 2021, *MNRAS*, 502, 564
 André, P., Men’shchikov, A., Bontemps, S., et al. 2010, *A&A*, 518, A102
 André, P., Di Francesco, J., Ward-Thompson, D., et al. 2014, *Protostars and Planets VI*, 27
 André, P., Revéret, V., Könyves, V., et al. 2016, *A&A*, 592, A54
 André, P., Arzoumanian, D., Könyves, V., Shimajiri, Y., & Palmeirim, P. 2019, *A&A*, 629, A4
 André, P., Palmeirim, P., & Arzoumanian, D. 2022, *A&A*, 667, A1
 Arzoumanian, D., André, P., Didelon, P., et al. 2011, *A&A*, 529, A6
 Arzoumanian, D., André, P., Peretto, N., & Könyves, V. 2013, *A&A*, 553, A119
 Arzoumanian, D., Shimajiri, Y., Inutsuka, S.-i., Inoue, T., & Tachihara, K. 2018, *PASJ*, 70, 96
 Arzoumanian, D., André, P., Könyves, V., et al. 2019, *A&A*, 621, A42
 Bergin, E. A., Alves, J., Huard, T., & Lada, C. J. 2002, *ApJ*, 570, L101
 Bohlin, R. C., Savage, B. D., & Drake, J. F. 1978, *ApJ*, 224, 132
 Bonne, L., Bontemps, S., Schneider, N., et al. 2020, *A&A*, 644, A27
 Chen, C.-Y., Mundy, L. G., Ostriker, E. C., Storm, S., & Dhabal, A. 2020, *MNRAS*, 494, 3675
 Chibueze, J. O., Omodaka, T., Handa, T., et al. 2014, *ApJ*, 784, 114
 Clarke, S. D., Whitworth, A. P., & Hubber, D. A. 2016, *MNRAS*, 458, 319
 Clarke, S. D., Whitworth, A. P., Duarte-Cabral, A., & Hubber, D. A. 2017, *MNRAS*, 468, 2489
 Clarke, S. D., Williams, G. M., Ibáñez-Mejía, J. C., & Walch, S. 2019, *MNRAS*, 484, 4024
 Cox, N. L. J., Arzoumanian, D., André, P., et al. 2016, *A&A*, 590, A110
 Dhabal, A., Mundy, L. G., Rizzo, M. J., Storm, S., & Teuben, P. 2018, *ApJ*, 853, 169
 Enokiya, R., Ohama, A., Yamada, R., et al. 2021, *PASJ*, 73, S256
 Federrath, C. 2016, *MNRAS*, 457, 375
 Fiege, J. D., & Pudritz, R. E. 2000, *MNRAS*, 311, 85
 Friesen, R. K., Bourke, T. L., Di Francesco, J., Gutermuth, R., & Myers, P. C. 2016, *ApJ*, 833, 204
 Gehman, C. S., Adams, F. C., & Watkins, R. 1996, *ApJ*, 472, 673
 Gibb, A. G. 2008, *Star Formation in NGC 2068, NGC 2071, and Northern L1630*, 4, 693
 Gong, M., & Ostriker, E. C. 2015, *ApJ*, 806, 31
 Hacar, A., & Tafalla, M. 2011, *A&A*, 533, A34
 Hacar, A., Kainulainen, J., Tafalla, M., Beuther, H., & Alves, J. 2016, *A&A*, 587, A97
 Hacar, A., Tafalla, M., Forbrich, J., et al. 2018, *A&A*, 610, A77
 Hacar, A., Clark, S., Heitsch, F., et al. 2022, in *Protostars and Planets VII*, eds. S. Inutsuka, et al., submitted [arXiv:2203.09562]
 Hennebelle, P., & André, P. 2013, *A&A*, 560, A68
 Henshaw, J. D., Kruijssen, J. M. D., Longmore, S. N., et al. 2020, *Nat. Astron.*, 4, 1064
 Hsieh, C.-H., Arce, H. G., Mardones, D., Kong, S., & Plunkett, A. 2021, *ApJ*, 908, 92
 Ikeda, N., Sunada, K., & Kitamura, Y. 2007, *ApJ*, 665, 1194
 Inutsuka, S.-I., & Miyama, S. M. 1992, *ApJ*, 388, 392
 Inutsuka, S.-I., & Miyama, S. M. 1997, *ApJ*, 480, 681
 Jackson, J. M., Finn, S. C., Chambers, E. T., Rathborne, J. M., & Simon, R. 2010, *ApJ*, 719, L185
 Kainulainen, J., Stutz, A. M., Stanke, T., et al. 2017, *A&A*, 600, A141
 Kashiwagi, R., & Tomisaka, K. 2021, *ApJ*, 911, 106
 Kawachi, T., & Hanawa, T. 1998, *PASJ*, 50, 577
 Könyves, V., André, P., Men’shchikov, A., et al. 2015, *A&A*, 584, A91

- Könyves, V., André, P., Arzoumanian, D., et al. 2020, *A&A*, **635**, A34
- Lada, C. J., Lada, E. A., Clemens, D. P., & Bally, J. 1994, *ApJ*, **429**, 694
- Lee, K. I., Fernández-López, M., Storm, S., et al. 2014, *ApJ*, **797**, 76
- Lin, S.-J., Shimajiri, Y., Hara, C., et al. 2016, *ApJ*, **826**, 193
- Marsh, K. A., Kirk, J. M., André, P., et al. 2016, *MNRAS*, **459**, 342
- Maruta, H., Nakamura, F., Nishi, R., Ikeda, N., & Kitamura, Y. 2010, *ApJ*, **714**, 680
- Matsumoto, T., Nakamura, F., & Hanawa, T. 1994, *PASJ*, **46**, 243
- Megeath, S. T., Gutermuth, R., Muzerolle, J., et al. 2012, *AJ*, **144**, 192
- Men'shchikov, A., André, P., Didelon, P., et al. 2012, *A&A*, **542**, A81
- Menten, K. M., Reid, M. J., Forbrich, J., & Brunthaler, A. 2007, *A&A*, **474**, 515
- Miville-Deschênes, M., Martin, P. G., Abergel, A., et al. 2010, *A&A*, **518**, A104
- Molinari, S., Swinyard, B., Bally, J., et al. 2010, *A&A*, **518**, A100
- Ntormousi, E., Hennebelle, P., André, P., & Masson, J. 2016, *A&A*, **589**, A24
- Onishi, T., Mizuno, A., Kawamura, A., Ogawa, H., & Fukui, Y. 1998, *ApJ*, **502**, 296
- Orkisz, J. H., Peretto, N., Pety, J., et al. 2019, *A&A*, **624**, A113
- Ostriker, J. 1964, *ApJ*, **140**, 1056
- Palmeirim, P., André, P., Kirk, J., et al. 2013, *A&A*, **550**, A38
- Panopoulou, G. V., Tassis, K., Goldsmith, P. F., & Heyer, M. H. 2014, *MNRAS*, **444**, 2507
- Panopoulou, G. V., Psaradaki, I., Skalidis, R., Tassis, K., & Andrews, J. J. 2017, *MNRAS*, **466**, 2529
- Panopoulou, G. V., Clark, S. E., Hacar, A., et al. 2022, *A&A*, **657**, A13
- Pattle, K., Fissel, L., Tahani, M., Liu, T., & Ntormousi, E. 2022, in *Protostars and Planets VII*, eds. S. Inutsuka et al., submitted [arXiv:2203.11179]
- Peretto, N., Gaudel, M., Louvet, F., et al. 2015, *EAS Publications Series*, **75**, 167
- Pety, J., Guzmán, V. V., Orkisz, J. H., et al. 2017, *A&A*, **599**, A98
- Pineda, J. E., Arzoumanian, D., André, P., et al. 2022, in *Protostars and Planets VII*, eds. S. Inutsuka et al., submitted [arXiv:2205.03935]
- Qian, L., Li, D., & Goldsmith, P. F. 2012, *ApJ*, **760**, 147
- Rosolowsky, E. W., Pineda, J. E., Kauffmann, J., & Goodman, A. A. 2008, *ApJ*, **679**, 1338
- Roy, A., André, P., Palmeirim, P., et al. 2014, *A&A*, **562**, A138
- Roy, A., André, P., Arzoumanian, D., et al. 2019, *A&A*, **626**, A76
- Sault, R. J., Teuben, P. J., & Wright, M. C. H. 1995, *ASP Conf. Ser.*, **77**, 433
- Schisano, E., Molinari, S., Elia, D., et al. 2020, *MNRAS*, **492**, 5420
- Schneider, S., & Elmegreen, B. G. 1979, *ApJS*, **41**, 87
- Schuller, F., André, P., Shimajiri, Y., et al. 2021, *A&A*, **651**, A36
- Shimajiri, Y., Kawabe, R., Takakuwa, S., et al. 2011, *PASJ*, **63**, 105
- Shimajiri, Y., Kitamura, Y., Saito, M., et al. 2014, *A&A*, **564**, A68
- Shimajiri, Y., Kitamura, Y., Nakamura, F., et al. 2015, *ApJS*, **217**, 7
- Shimajiri, Y., André, P., Braine, J., et al. 2017, *A&A*, **604**, A74
- Shimajiri, Y., André, P., Ntormousi, E., et al. 2019a, *A&A*, **632**, A83
- Shimajiri, Y., André, P., Palmeirim, P., et al. 2019b, *A&A*, **623**, A16
- Sousbie, T. 2011, *MNRAS*, **414**, 350
- Sousbie, T., Pichon, C., & Kawahara, H. 2011, *MNRAS*, **414**, 384
- Tafalla, M., & Hacar, A. 2015, *A&A*, **574**, A104
- Tafalla, M., Myers, P. C., Caselli, P., Walmsley, C. M., & Comito, C. 2002, *ApJ*, **569**, 815
- Tafalla, M., Myers, P. C., Caselli, P., & Walmsley, C. M. 2004, *A&A*, **416**, 191
- Tomisaka, K. 2014, *ApJ*, **785**, 24
- Williams, G. M., Peretto, N., Avison, A., Duarte-Cabral, A., & Fuller, G. A. 2018, *A&A*, **613**, A11
- Wilner, D. J. & Welch, W. J. 1994, *ApJ*, **427**, 898
- Yonekura, Y., Asayama, S., Kimura, K., et al. 2005, *ApJ*, **634**, 476
- Zhang, G.-Y., André, P., Men'shchikov, A., & Wang, K. 2020, *A&A*, **642**, A76

Appendix A: Complementary figures

Figure A.1 indicates the area of each figure used in this paper. Figure A.2 shows a comparison of the velocity channel maps of i) NOEMA $\text{H}^{13}\text{CO}^+(1-0)$ data, ii) Nobeyama $\text{H}^{13}\text{CO}^+(1-0)$ data, iii) data combined the NOEMA data with the Nobeyama data (hereafter, called NOEMA+45m data), and iv) NOEMA+45m data smoothed to the angular resolution of the Nobeyama $\text{H}^{13}\text{CO}^+(1-0)$ data. Figure A.3 shows a comparison of the *Herschel* H_2 column density map, Nobeyama 45m C^{18}O integrated intensity map, and Nobeyama 45m H^{13}CO^+ integrated intensity map. Figure A.4 shows a pixel-to-pixel correlation plot between Nobeyama H^{13}CO^+ , Nobeyama C^{18}O , and *Herschel* H_2 column density data.

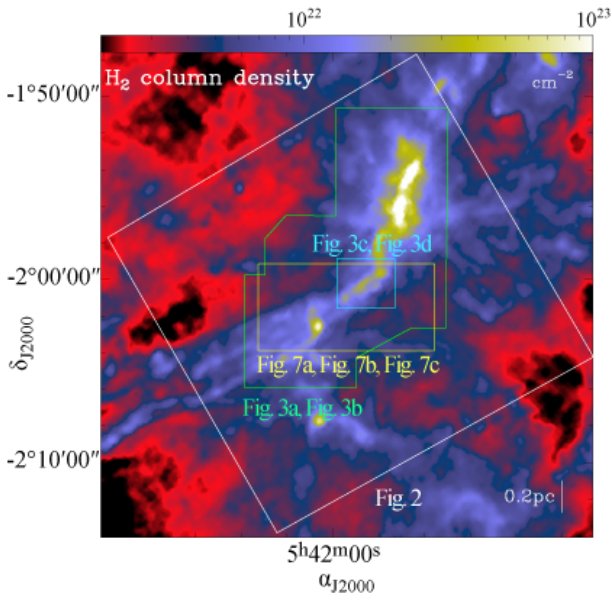


Fig. A.1. *Herschel* column density map, with the area of each figure indicated. A white box indicates the area shown in Fig. 2. A green polygon indicates the area shown in Fig. 4a and Fig. 4b. A yellow box indicates the area shown in Fig. 7a, Fig. 7b, and Fig. 7c. A cyan box indicates the area shown in Fig. 4c and Fig. 4d.

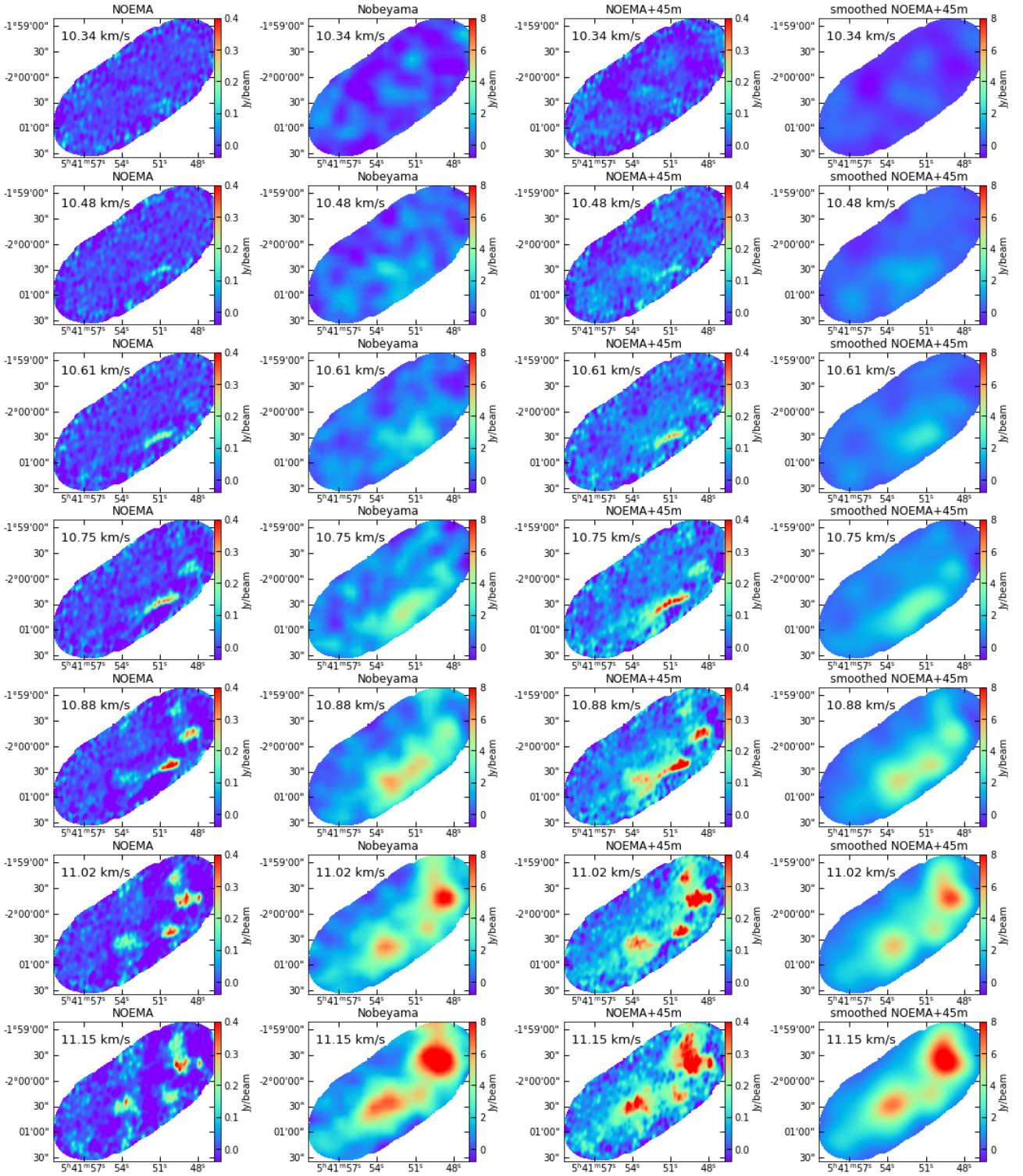


Fig. A.2. Comparison of the velocity channel maps of NOEMA $\text{H}^{13}\text{CO}^+(1-0)$ data (first column), Nobeyama $\text{H}^{13}\text{CO}^+(1-0)$ data (second column), NOEMA+45m data (third column), and smoothed NOEMA+45m data (fourth column). The velocity is indicated at the top left of each panel.

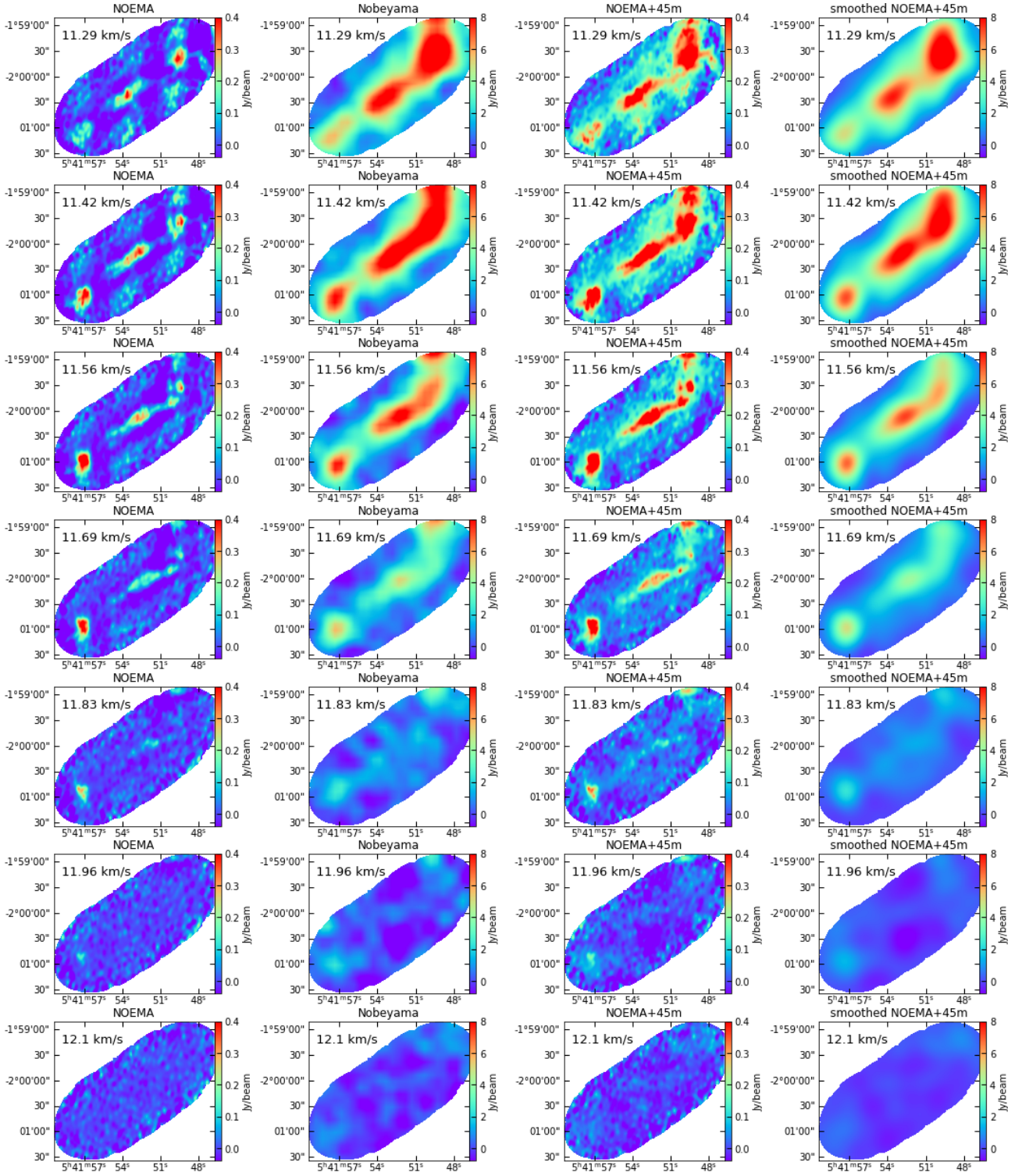


Fig. A.2. (continued.)

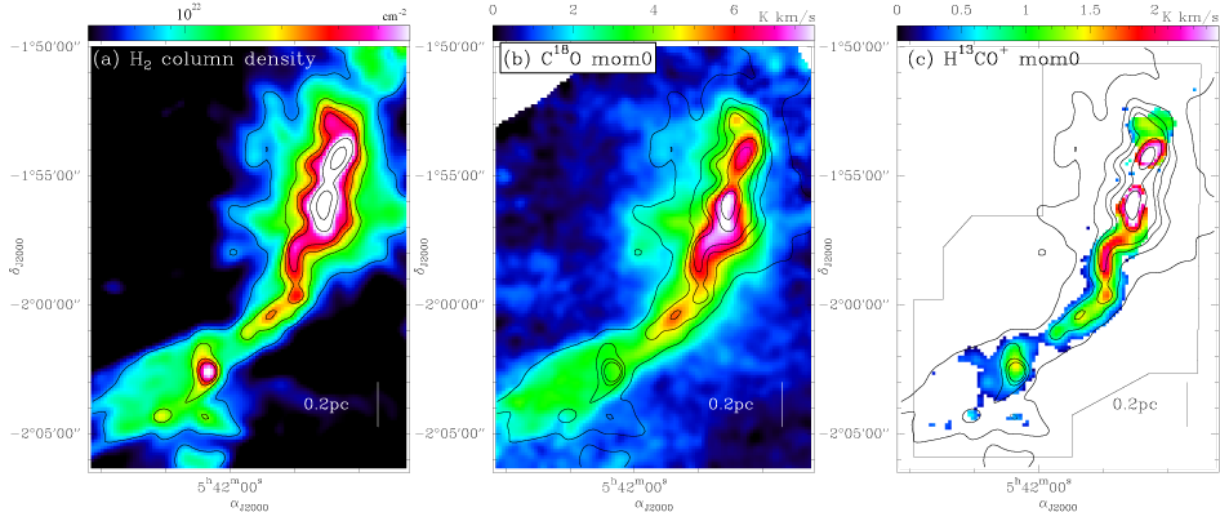


Fig. A.3. Comparison of (a) *Herschel* H_2 column density, (b) Nobeyama 45m C^{18}O integrated intensity, and (c) Nobeyama 45m H^{13}CO^+ (1–0) integrated intensity maps with an angular resolution of $30''$. Panel a is the same as Fig. 1, but the angular resolution is smoothed to be $30''$. Panel b is the same as Fig. 2m, but the angular resolution is smoothed to be $30''$. Panel c is the same as Fig. 4b. The black contours in each panel indicate the A_V column density levels of 8, 16, 24, 32, 64, 128, and 256 mag (assuming $N_{\text{H}_2}/A_V = 0.94 \times 10^{21} \text{ cm}^{-2}$; Bohlin et al. 1978).

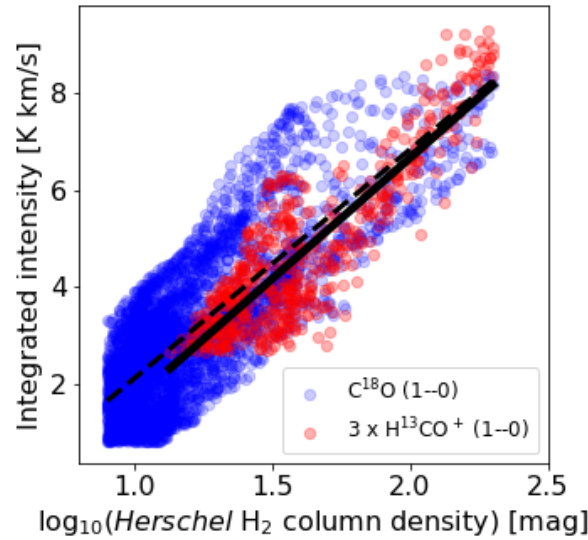


Fig. A.4. Pixel-to-pixel correlation between H^{13}CO^+ (1–0) and C^{18}O (1–0) integrated intensities in K km s^{-1} and *Herschel* H_2 column density in mag (assuming $N_{\text{H}_2}/A_V = 0.94 \times 10^{21} \text{ cm}^{-2}$, Bohlin et al. 1978). The blue and red points indicate the correlation between C^{18}O (1–0) integrated intensity and *Herschel* H_2 column density and between H^{13}CO^+ (1–0) integrated intensity and *Herschel* H_2 column density, respectively. The dashed and solid lines indicate the best-fit result for the C^{18}O - *Herschel* H_2 column density correlation and for the H^{13}CO^+ - *Herschel* H_2 column density correlation.

Appendix B: Comparison of the median radial profiles between the 8'' resolution ArTéMiS+*Herschel* and 18'2 resolution *Herschel* column density maps

For comparison with Fig. 6 obtained from 8''-resolution ArTéMiS+*Herschel* data, Fig. B.2 shows the median radial profiles of the NGC 2024S filament derived from the 18'2-resolution *Herschel* column density map of Fig. 1. Despite the difference in angular resolution (Table 8), the *Herschel* and ArTéMiS+*Herschel* radial profiles and corresponding width measurements are consistent with each other (see André et al. 2022 for a detailed discussion for the effect of resolution on filament width measurements).

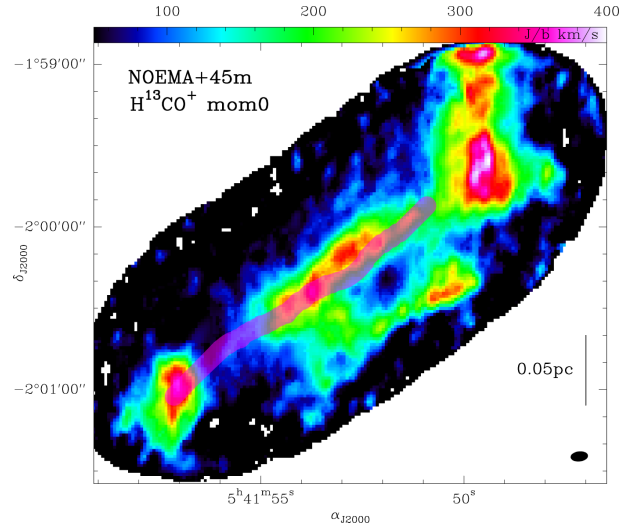


Fig. B.1. Filament crest on the NOEMA+45m H¹³CO⁺(1–0) integrated intensity maps. The filament crest is determined by the DisPerSE algorithm (Sousbie 2011; Sousbie et al. 2011; Arzoumanian et al. 2011) and is used for producing the median radial profiles shown in Figs. 6 and B.2.

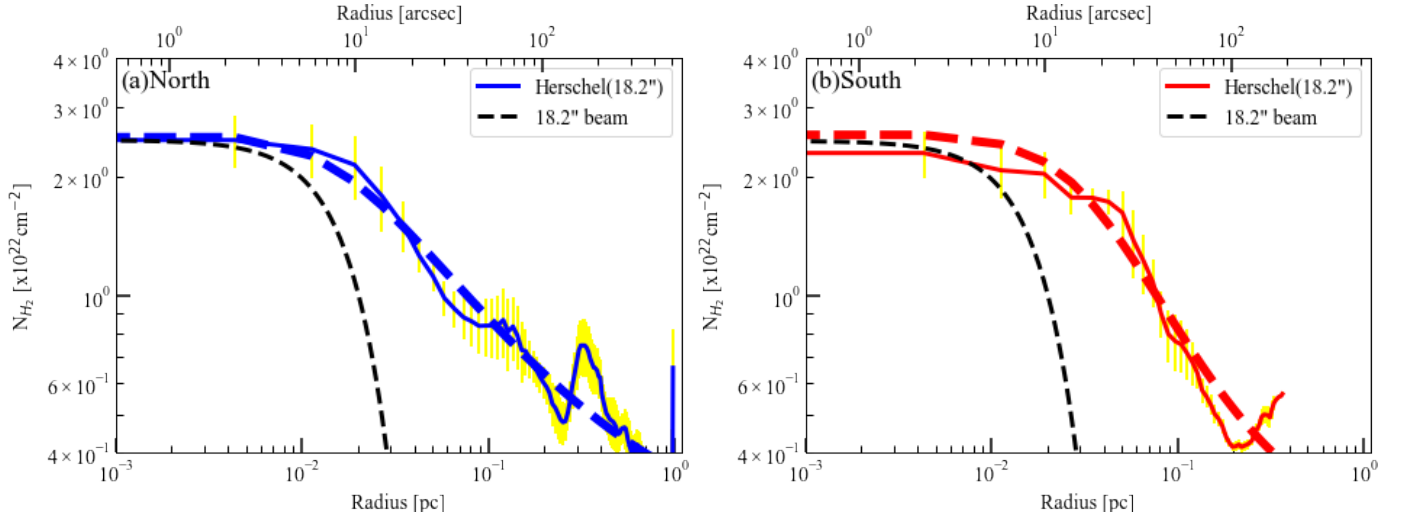


Fig. B.2. Median radial *Herschel* column density profiles for the northeastern (a) and southwestern (b) side of the NGC 2024S filament. The defined crest of the filament is shown in Fig. B.1. The dashed black curves indicate the angular resolution of the *Herschel* column density map (18''). The dashed curves show the best-fit Plummer mode. The yellow bars show the dispersion ($\pm 1\sigma$) of the distribution of the radial profile along the filament. The area affected by the secondary component seen in NOEMA H^{13}CO^+ is avoided to produce the median radial profile for the southwestern side of the NGC 2024S filament (see Sect. 3.1.3).